Geochemistry Geophysics Geosystems G3
AN ELECTRONIC JOURNAL OF THE EARTH SCIENCES
Published by AGU and the Geochemical Society

Article
Volume 9, Number 8
2 August 2008
Q08O10, doi:10.1029/2008GC001965
ISSN: 1525-2027

Magmatic and tectonic extension at mid-ocean ridges: 1. Controls on fault characteristics

Mark D. Behn
Department of Geology and Geophysics, Woods Hole Oceanographic Institution, 360 Woods Hole Road, MS #22, Woods Hole, Massachusetts 02543, USA (mbehn@whoi.edu)

Garrett Ito
Department of Geology and Geophysics, SOEST, University of Hawaii, 1680 East-West Road, POST 810, Honolulu, Hawaii 96822, USA (gito@hawaii.edu)

[1] We use 2-D numerical models to explore the thermal and mechanical effects of magma intrusion on fault initiation and growth at slow and intermediate spreading ridges. Magma intrusion is simulated by widening a vertical column of model elements located within the lithosphere at a rate equal to a fraction, M, of the total spreading rate (i.e., $M = 1$ for fully magmatic spreading). Heat is added in proportion to the rate of intrusion to simulate the thermal effects of magma crystallization and the injection of hot magma into the crust. We examine a range of intrusion rates and axial thermal structures by varying M, spreading rate, and the efficiency of crustal cooling by conduction and hydrothermal circulation. Fault development proceeds in a sequential manner, with deformation focused on a single active normal fault whose location alternates between the two sides of the ridge axis. Fault spacing and heave are primarily sensitive to M and secondarily sensitive to axial lithosphere thickness and the rate that the lithosphere thickens with distance from the axis. Contrary to what is often cited in the literature, but consistent with prior results of mechanical modeling, we find that thicker axial lithosphere tends to reduce fault spacing and heave. In addition, fault spacing and heave are predicted to increase with decreasing rates of off-axis lithospheric thickening. The combination of low M, particularly when M approaches 0.5, as well as a reduced rate of off-axis lithospheric thickening produces long-lived, large-offset faults, similar to oceanic core complexes. Such long-lived faults produce a highly asymmetric axial thermal structure, with thinner lithosphere on the side with the active fault. This across-axis variation in thermal structure may tend to stabilize the active fault for longer periods of time and could concentrate hydrothermal circulation in the footwall of oceanic core complexes.

Components: 12,897 words, 14 figures, 1 table.

Keywords: mid-ocean ridges; faulting; magmatism; numerical modeling.

Index Terms: 3035 Marine Geology and Geophysics: Midocean ridge processes; 8118 Tectonophysics: Dynamics and mechanics of faulting (8004); 8145 Tectonophysics: Physics of magma and magma bodies.

Received 29 January 2008; **Revised** 7 May 2008; **Accepted** 15 May 2008; **Published** 2 August 2008.

Behn, M. D., and G. Ito (2008), Magmatic and tectonic extension at mid-ocean ridges: 1. Controls on fault characteristics, *Geochem. Geophys. Geosyst.*, *9*, Q08O10, doi:10.1029/2008GC001965.

Theme: Formation and Evolution of Oceanic Crust Formed at Fast Spreading Rates

1. Introduction

[2] The style of tectonic faulting at mid-ocean ridges is highly sensitive to spreading rate, with slow spreading ridges characterized by larger and more widely spaced faults than fast spreading ridges [*Searle and Laughton*, 1981; *Macdonald*, 1982; *Goff*, 1991; *Goff et al.*, 1997; *Small*, 1998]. The dependence of fault style on spreading rate is typically attributed to changes in the mechanical strength of the lithosphere caused by differences in the axial thermal structure, with overall cooler crust at slow spreading compared to fast and intermediate spreading ridges [*Shaw*, 1992; *Malinverno and Cowie*, 1993; *Shaw and Lin*, 1993, 1996]. On a regional scale, magma supply also influences axial thermal structure [*Sleep*, 1975; *Neumann and Forsyth*, 1993; *Phipps Morgan and Chen*, 1993; *Shaw and Lin*, 1996] and this influence has been thought to cause rapid variations in fault characteristics and axial morphology along ridges with relatively constant spreading rates (e.g., Galápagos Spreading Center [*Canales et al.*, 1997; *Detrick et al.*, 2002; *Sinton et al.*, 2003; *Blacic et al.*, 2004], Juan de Fuca Ridge [*Canales et al.*, 2005], Lau Spreading Center [*Martinez et al.*, 2006], and Southeast Indian Ridge [*Goff et al.*, 1997]).

[3] A correlation between fault style and magma supply is also observed along individual slow spreading ridge segments. Residual gravity anomalies [*Kuo and Forsyth*, 1988; *Lin et al.*, 1990; *Detrick et al.*, 1995] and seismic refraction data [*Tolstoy et al.*, 1993; *Canales et al.*, 2000; *Hooft et al.*, 2000; *Hosford et al.*, 2001] indicate that many slow spreading segments are characterized by along-axis variations in crustal thickness, with thicker crust near the segment center and thinner crust toward the segment ends. These variations in crustal thickness correspond to along-axis changes in fault style, with small, closely spaced faults at the segment center and larger, more widely spaced faults near the segment ends [*Shaw*, 1992; *Shaw and Lin*, 1993; *Escartín et al.*, 1999; *Hooft et al.*, 2000]. Thermal models that simulate focused magma supply toward segment centers predict the crust to be warmer in these regions than at segment ends [*Phipps Morgan and Forsyth*, 1988; *Shen and Forsyth*, 1992; *Behn et al.*, 2007], and this thermal structure has been invoked to cause the segment-scale variations in faulting [*Shaw*, 1992; *Shaw and Lin*, 1993, 1996].

[4] The inferred relationship between fault style, magma supply, and axial thermal structure is based on the premise that colder, thicker axial lithosphere can support longer lived faults that accumulate greater throw and are transported farther off-axis before a new fault is created at the ridge axis. This positive scaling between fault throw and lithospheric thickness is derived from a flexural model for lithospheric deformation, in which the stress near the fault is calculated assuming the lithosphere behaves as an elastic beam [e.g., *Forsyth*, 1992]. However, studies that incorporate a more realistic elastic-plastic rheology for the oceanic lithosphere show the opposite relationship, with fault offset increasing with decreasing lithospheric thickness [*Buck*, 1993; *Lavier et al.*, 2000]. These predictions therefore present an inconsistency when interpreting the observed variations in ridge fault style solely in terms of differences in lithospheric thickness.

[5] A shortcoming of most previous models for fault evolution is that they focused on the effects of magma supply and spreading rate on ridge thermal structure, but did not integrate the mechanical effects of dike injection. Dikes are well known to strongly influence the local stress field [*Mastin and Pollard*, 1988; *Rubin and Pollard*, 1988; *Curewitz and Karson*, 1998; *Behn et al.*, 2006] and can even generate normal faulting, subsidence, and graben formation in volcanic rift zones [e.g., *Abdallah et al.*, 1979; *Sigurdsson*, 1980; *Pollard et al.*, 1983; *Rubin*, 1992; *Hofton and Foulger*, 1996; *Bull et al.*, 2003; *Wright et al.*, 2006]. Thus, variations in the rate and depth distribution of dikes at the ridge axis will likely influence the style of faulting [*Chadwick and Embley*, 1998; *Carbotte et al.*, 2006]. In particular, the longevity of slip on normal faults has been linked to the rate of magma accretion at the ridge axis [*Buck et al.*, 2005; *Tucholke et al.*, 2008].

[6] The goal of this study is to explore the relationship between magmatic and tectonic extension, axial thermal structure, and faulting at mid-ocean ridges. To do so, we develop a 2-D elastic-viscoplastic model for dike injection that accounts for both the thermal and mechanical effects of dike intrusion. On the basis of our numerical results we quantify the relationship between axial thermal structure, magma accretion rate, fault throw, and fault spacing. We find that fault throw and spacing increase for decreasing lithospheric thickness, decreasing rates of off-axis lithospheric thickening, and most importantly, for decreasing rates of magma accretion. Our results imply that magma supply influences faulting style predominantly by modulating the amount of magmatic extension, while the

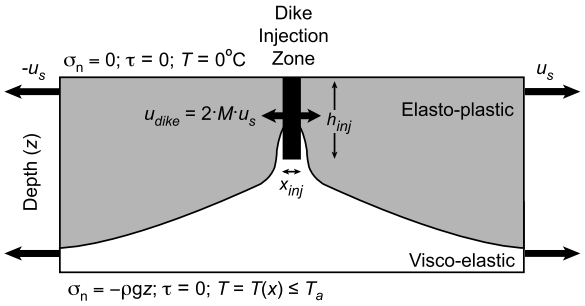

Figure 1. Model setup used for numerical simulations of magmatic spreading at a mid-ocean ridge. The dike injection zone is illustrated with the thick black line. Gray region represents the portion of the model space that experiences brittle deformation, while the white region behaves viscously. Deformation is driven by applying a uniform half-spreading rate, u_s, to either side of the model space. The rate of magma injection is controlled by the parameter M, which is defined as the fraction of the total spreading rate accommodated by magma accretion; σ_n and τ denote normal and shear stress boundary conditions, respectively, and T is temperature.

effects of axial thermal structure are secondary and more complex than often cited.

2. Model for Magma Intrusion at Mid-Ocean Ridges

2.1. Conceptual Model

[7] Seafloor spreading at mid-ocean ridges is accommodated through a combination of dike intrusion and tectonic faulting. Diking is typically focused within a 5–10 km neovolcanic zone at the ridge axis, with active faulting localized around the neovolcanic zone [*Ballard and van Andel*, 1977; *Macdonald*, 1986; *Macdonald and Fox*, 1988; *Smith and Cann*, 1993; *Hooft et al.*, 1996]. Because dikes advect mass and heat vertically and laterally through the crust, they have the potential to influence near ridge faulting by altering both the axial lithospheric structure and the local stress field. Here we simulate the effects of magma intrusion at an idealized 2-D spreading ridge assuming a constant spreading rate and uniform depth distribution of intrusion (Figure 1). Although diking is a stochastic process, we approximate its long-term influence by assuming a constant injection rate with time. In our companion paper [*Ito and Behn*, 2008] we relax this condition and evaluate how temporal variations in the rate of magma intrusion affect faulting and the evolution of axial morphology. The rate of magma intrusion is described by the parameter M, which is defined as the fraction of the total spreading rate accommodated by magma accretion [e.g., *Buck et al.*, 2005; *Behn et al.*, 2006]. Thus, $M = 1$ corresponds to the case where the rate of dike opening is equal to the full spreading rate and $M = 0$ represents purely amagmatic spreading. Heat associated with the injection temperature of the magma and the latent heat of crystallization [*Sleep*, 1975; *Phipps Morgan and Chen*, 1993] is added to the ridge axis in proportion to the rate of intrusion.

2.2. Mathematical and Numerical Formulation

[8] We use the Fast Lagrangian Analysis of Continua (FLAC) technique [*Cundall*, 1989; *Poliakov et al.*, 1993] to solve the equations of conservation of mass and momentum in a visco-elastic-plastic continuum (see Appendix A1). This explicit hybrid finite element-finite difference approach has been used to simulate localized deformation (i.e., faulting) in a variety of extensional environments [e.g., *Hassani and Chéry*, 1996; *Poliakov and Buck*, 1998; *Lavier et al.*, 2000; *Behn et al.*, 2006] and is described in detail elsewhere [*Poliakov et al.*, 1993; *Lavier and Buck*, 2002]. Dike intrusion is simulated kinematically by uniformly widening a vertical column of elements at the center of the model space at a rate, u_{dike} (Figure 1). Dike opening is achieved numerically by relating the stresses in the dike elements, σ_{ij}^{dike}, to the horizontal strain, ε_{xx}^{dike}, by

$$\sigma_{xx}^{dike} = \varepsilon_{xx}^{dike}\left(\frac{E(\nu-1)}{(\nu+1)(1-2\nu)}\right) \tag{1a}$$

$$\sigma_{zz}^{dike} = \frac{\nu\sigma_{xx}^{dike}}{(1-\nu)} \tag{1b}$$

$$\sigma_{yy}^{dike} = \nu\left(\sigma_{xx}^{dike} + \sigma_{zz}^{dike}\right) \tag{1c}$$

$$\sigma_{xz}^{dike} = 0 \tag{1d}$$

where ν is Poisson's ratio, $\varepsilon_{xx}^{dike} = u_{dike}dt/x_{inj}$, u_{dike} is the widening rate of the dike, x_{inj} is the width of the injection zone, and dt is the length of the time step. This approach allows the location of the dike zone to evolve with the deforming mesh and eliminates the need to impose nodal velocities explicitly on the dike elements.

Table 1. Summary of Model Parameters

Variable	Meaning	Value	Units
C	cohesion		MPa
C_o	initial cohesion	44	MPa
$C_{\min}$	minimum cohesion	4	MPa
C_p	specific heat of magma	1000	J kg^{-1} °C^{-1}
E	Young's modulus	30×10^9	Pa
F_c	crystal fraction = $(T_{liq} - T)/(T_{liq} - T_{sol})$	0–1	—
h_{inj}	injection zone height	6.0	km
H	lithospheric thickness		km
H_o	axial lithosphere thickness, i.e., depth to 600°C	3–9	km
L	latent heat of crystallization	5×10^5	J kg^{-1}
M	fraction of spreading accommodated by accretion	0.5–1	—
Nu	efficiency of hydrothermal circulation	4–8	—
T_a	asthenosphere temperature	1300	°C
T_{sol}	solidus temperature of basalt	1000	°C
T_{liq}	liquidus temperature of basalt	1300	°C
u_{AF}, u_{IF}	velocity of active and inactive faults		cm a^{-1}
u_s	half spreading rate	1–2.5	cm a^{-1}
x_{AF}	distance an active fault migrates away from the axis		km
x_{inj}	injection zone width	0.25	km
μ	friction coefficient	0.6	—
Δs_c	critical slip for total cohesion loss	0.5	km
ΔS	fault spacing		km
Δt	lifetime of active fault		years
Δx	total fault heave		km
ϕ_{lith}	off-axis slope of lithosphere	10–30	°
θ	fault dip		°
ν	Poisson's ratio	0.25	—
κ	base thermal conductivity	2.5	W m^{-1} K^{-1}
ρ	density	3300	kg m^{-3}

[9] Temperature evolution is modeled using a Lagrangian formulation, so heat advection occurs with the deforming grid. At each time step we use explicit finite differences to solve for the diffusion of heat with sources (see Appendix A2 for derivation),

$$\frac{DT}{Dt} = \begin{cases} \nabla \cdot (\kappa \nabla T) & (T \geq T_{liq}) \\ \nabla \cdot \left[\dfrac{\kappa}{\left(1 + \dfrac{L}{C_P(T_{liq} - T_{sol})}\right)} \nabla T \right] + (T_{liq} - T)\dfrac{u_{dike}}{x_{inj}} & (T_{liq} > T \geq T_{sol}) \\ \nabla \cdot (\kappa \nabla T) + \left[(T_{liq} - T) + \dfrac{L}{C_p} \right] \dfrac{u_{dike}}{x_{inj}} & (T \leq T_{sol}) \end{cases} \quad (2)$$

where T is temperature and C_p is heat capacity. The three temperature intervals are needed to simulate the heat carried by the injected magma as well as the latent heat (L) with crystallization in which crystal fraction is assumed to increase linearly with decreasing T between the magma liquidus (T_{liq}) and solidus (T_{sol}). No magmatic or latent heat (per kg) is added in the first (top) interval, magmatic and latent heat are added and crystallinity changes with T in the second interval, and all of the magmatic and latent heat are added in the third interval. The effects of hydrothermal circulation are simulated by increasing effective diffusivity, κ, by a factor, Nu, in regions of the model space above a threshold depth of 7 km and where $T < 600$°C [e.g., *Phipps Morgan et al.*, 1987].

[10] Material behavior is a function of the thermal structure, stress, and accumulated plastic strain

(Appendix A3). In regions where deformation is visco-elastic, the material behaves as a Maxwell solid. Viscous deformation is incompressible and follows a non-Newtonian temperature and strain rate dependent power law [*Kirby*, 1983; *Chen and Morgan*, 1990; *Kohlstedt et al.*, 1995]. Material properties appropriate for a dry diabase rheology [*Mackwell et al.*, 1998] are assumed throughout the model space. Plastic yielding is controlled by Mohr-Coulomb theory, in which cohesion is a function of the total accumulated plastic strain [*Poliakov and Buck*, 1998]. Cohesion, C, decreases linearly with the total accumulated plastic strain from its initial value, C_o, to a minimum, $C_{\min}$, over a fault offset Δs_c [*Lavier et al.*, 2000]. Unless noted in the text we assume values of C_o, $C_{\min}$, and Δs_c equal to 44 MPa, 4 MPa, and 500 m, respectively (see Table 1 for a list of all model parameters).

2.3. Model Domain and Boundary Conditions

[11] The numerical domain is 60 km wide by 20 km deep, with a grid spacing that is smallest (0.25 km × 0.25 km) at the ridge axis and coarsens with distance from the ridge (0.75 km × 1 km at the lower left/right corners of the box). Deformation is driven by imposing a uniform far-field extension rate along the edges of the model space with a half-spreading velocity, u_s (Figure 1). The injection zone is situated at the ridge axis and extends from the surface down to a depth h_{inj} (Figure 1). The rate of dike opening, u_{dike}, is controlled by the parameter M such that $u_{dike} = 2 \cdot M \cdot u_s$. A hydrostatic boundary condition is assumed for the base of the model space and the top boundary is stress free. The top of the model space is set to 0°C, while the bottom temperature is set equal to the steady state solution for a cooling half-space at the depths coinciding to the model base and with a maximum asthenosphere temperature (T_a) of 1300°C. All models are run for a sufficient model time that all lithosphere was created at the axis during the model run (e.g., 30 km/u_s or 3 Ma for u_s = 1 cm/a).

3. A Simple Model for Sequential Faulting at Mid-Ocean Ridges

[12] To analyze the basic cause for the behavior of our numerical models we first examine a more simplified set of calculations. Faulting at mid-ocean ridges is often assumed to occur sequentially, with the majority of tectonic extension focused on a single fault at any given time [e.g., *Shaw and Lin*, 1993]. In such a model, faults initiate near the ridge axis and are rafted off-axis until the stress required to continue to slip on the initial fault exceeds the stress required to break a new fault (Figure 2). Numerical studies show that in most cases the new fault will be antithetic and form on the opposite side of the ridge axis from the original fault [e.g., *Melosh and Williams*, 1989; *Poliakov and Buck*, 1998]. This results in asymmetric rates of off-axis fault transport on either side of the ridge axis, with the active fault migrating away from the axis at a rate, $u_{AF} = 2u_s(M - 0.5)$, and the inactive fault migrating at a rate $u_{IF} = u_s$ [*Buck et al.*, 2005]. This sequential style of fault initiation and asymmetric off-axis migration implies that total fault heave, Δx, is a simple function of M and the distance the active fault is transported off-axis before the formation of the new fault, x_{AF} [*Buck et al.*, 2005]

$$\Delta x = \frac{(1 - M)}{(M - 0.5)} x_{AF}. \tag{3}$$

Assuming that a fault migrates a distance, x_{AF} while it is active plus a distance $u_s(x_{AF}/u_{AF})$ until the next fault on the same plate forms (Figure 2), the fault spacing, ΔS, is

$$\Delta S = \frac{M}{(M - 0.5)} x_{AF}. \tag{4}$$

The distance, x_{AF}, that a fault will remain active depends on a combination of factors, including lithospheric thickness (H), the off-axis slope of the lithosphere (ϕ_{lith}), fault dip (θ), and the frictional properties of the lithosphere. Thus, observations of fault spacing and fault heave reflect upon the rate of magma injection (M) as well as the material properties of the oceanic lithosphere.

[13] To compare equations (3) and (4) with predictions from our numerical models below, we compute x_{AF} by following the concepts of previously proposed force-balance models [e.g., *Forsyth*, 1992; *Buck*, 1993; *Lavier et al.*, 2000]. These models assume that the depth-integrated tensile stress (here and in Appendix B we are referring to the nonlithostatic stress) required to keep an existing fault active equals or exceeds the depth-integrated stress to break a new fault near the ridge axis. We assume the net pulling forces needed to keep a fault slipping are those associated with friction and reduced cohesion (C) on the fault, F_F, and those associated with bending an elasto-plastic lithosphere around the fault F_B [*Buck*, 1993;

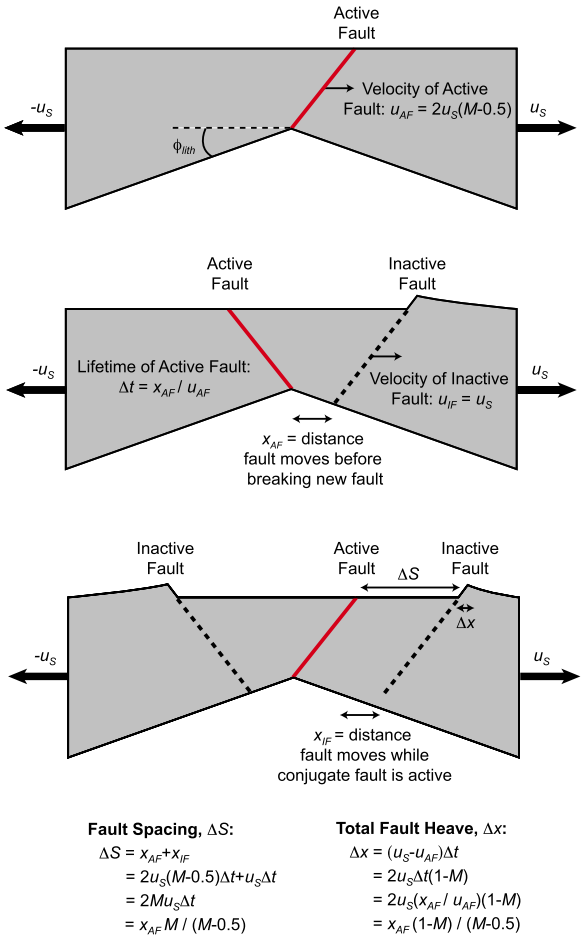

Figure 2. Schematic model for sequential fault development at mid-ocean ridges. Active faulting (red) occurs on one side of the ridge axis until the stress required to continue slip on the active fault exceeds that required to break a new fault nearer the ridge axis. This model predicts that both fault spacing, ΔS, and total fault heave, Δx, can be predicted from the fraction of magmatic extension, M, and the distance, x_{AF}, that the active fault migrates off-axis before breaking a new fault. ϕ_{lith} denotes the off-axis slope of the base of the lithosphere, which in the numerical models is defined at the 600°C isotherm. In runs with a fixed thermal structure, ϕ_{lith} is imposed as a linear gradient; in runs with thermal evolution, ϕ_{lith} is calculated from the resulting thermal structure.

Lavier et al., 2000]. The strength of the unfaulted, axial lithosphere F_I is supplied by friction as well as the full cohesion (C_0). Hence, the criteria for forming a new fault (which determines x_{AF}) is

$$F_F + F_B \geq F_I. \quad (5)$$

While F_I remains constant, the other two change off-axis as lithospheric thickness H and fault heave Δx increase and fault dip θ decreases (Figure 3). Specifically, F_F decreases quickly owing to the loss of cohesion with fault slip, and causes the fault to become weak and remain active for a period time. However, once cohesion is fully reduced, F_F and F_B increase slowly with distance x as the fault moves into increasingly thick lithosphere, until eventually (equation (5)) is achieved at $x = x_{AF}$ and a new fault forms on the opposite plate.

4. Numerical Models of Fault Development at Mid-Ocean Ridges

4.1. Fixed Ridge Thermal Structure

[14] To investigate the influence of lithospheric structure on fault style, we conducted a series of model runs with a fixed axial thermal structure. At the ridge axis, temperature was imposed to increase linearly with depth from 0°C at the surface to 600°C at a depth H_o (representing the approximate depth of the brittle-ductile transition). Below H_o temperature increases rapidly to the asthenospheric temperature (1300°C) over a depth interval of 0.5 km. An important aspect of this set of calculations was that we imposed a linear increase in

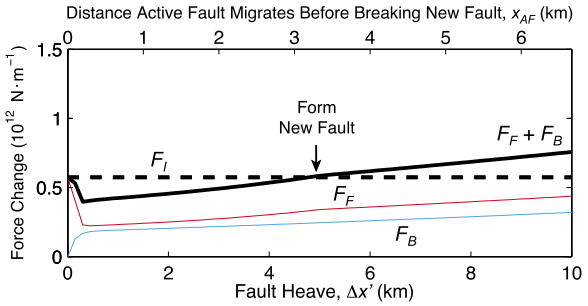

Figure 3. Calculation of the depth-integrated tensile strength due to friction on the active fault, F_F (thin red line), depth-integrated tensile strength associated with bending an elasto-plastic layer due to slip on the fault, F_B (thin blue line), and depth-integrated tensile strength of unfaulted lithosphere, F_I (thick dashed line), as a function of fault heave, $\Delta x'$, for $H_o = 6$ km and $M = 0.7$. Note that total fault heave is related to the distance the fault has migrated off-axis (x_{AF}) through equation (3). F_F initially decreases owing to cohesion loss on the active fault surface and then increases owing to the off-axis thickening of the lithosphere. F_B increases with heave $\Delta x'$ as elastic bending stresses accumulate in the lithosphere. The force required to continue extension on the active fault ($F_F + F_B$, thick solid line) exceeds F_I when $\Delta x' \sim 4.9$ km, corresponding to $x_{AF} \sim 3.3$ km.

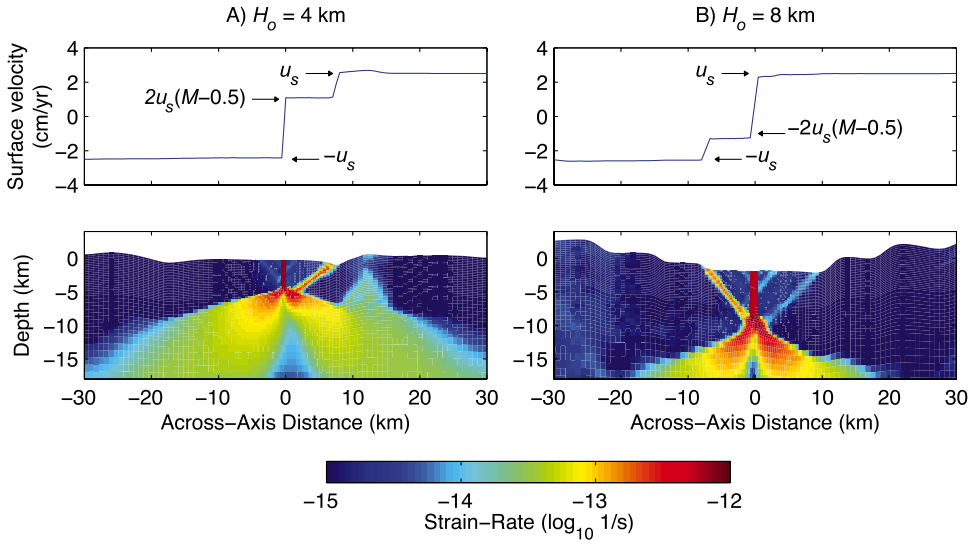

Figure 4. Model results after 1 Ma of deformation for two cases with $M = 0.7$ and (a) $H_o = 4$ km and (b) $H_o = 8$ km. Top panels show horizontal surface velocity; bottom panels show second invariant of the strain rate tensor. High strain rates within the lithosphere are found along the active fault and within the dike injection zone. Surface velocity of the active fault follows kinematic prediction of *Buck et al.* [2005]. Note that faults have greater heave and are more widely spaced in the case with thinner lithosphere ($H_o = 4$ km).

lithospheric thickening off-axis with a slope that was proportional to the on-axis thickness H_o, i.e., the lithosphere doubled in thickness over 20 km. The maximum depth of seismicity at the Mid-Atlantic Ridge ranges from 3 to 9 km [*Toomey et al.*, 1988; *Kong et al.*, 1992; *Wolfe et al.*, 1995; *Barclay et al.*, 2001], and seismic moment release studies [*Solomon et al.*, 1988] and estimates of cumulative fault slip [*Escartín et al.*, 1999] indicate that 70–90% of spreading is accommodated by magmatic intrusion. Thus, we first examined a series of runs for $H_o = 3$–9 km with $M = 0.7$ for a half spreading rate $u_s = 2.5$ cm/a. The height of the magma injection zone was set to be equal to the axial lithospheric thickness ($h_{inj} = H_o$).

[15] In all cases, faults initiate near the axis where the lithosphere is thinnest and are subsequently rafted off-axis by continued magma accretion (Figure 4). This style of fault initiation and migration is consistent with the sequential fault model shown in Figure 2, with a single fault actively accumulating slip at any time. Fault heave (Δx) and spacing (ΔS) are estimated from the average value of each quantity for all faults formed during a model run. Comparing cases with $H_o = 3$–9 km, we find that faults formed in thinner axial lithosphere accumulate greater slip and are more widely spaced than those formed in thicker lithosphere (Figures 5 and 6a–6c). These results contrast with the predictions of a purely elastic lithosphere, which predicts $\Delta x \sim H^{1/4}$ [*Forsyth*, 1992], but are consistent with the scaling for an elastic-plastic layer [*Buck*, 1993; *Lavier et al.*, 2000] (and hence our use of their scaling for F_B).

[16] A prediction of our numerical models that is important to the force-balance calculations is that fault dip decreases with increasing fault heave (Figure 7). Initially, fault dip (θ) is controlled by the coefficient of friction as predicted by Mohr-Coulomb theory, and is ~55° in our calculations where $\mu = 0.6$. As slip accumulates on the fault, θ decreases to a minimum value of ~30–35° over a heave of ~4 km and then remains nearly constant thereafter. This behavior appears to be consistent over a range of H_o and M (Figure 7). To account for this effect in the force-balance model, we assume a linear decrease in θ with Δx. Figure 6c compares the final dip angle measured in the numerical runs with that predicted by the force-balance model. Comparing the predictions of fault heave and spacing from the force-balance model to our numerical results, we find that the force-balance model provides a good fit, slightly over-predicting fault spacing for thin axial lithosphere (Figures 6a and 6b).

[17] In the next set of model calculations we examine the effect of lithospheric slope (ϕ_{lith}) on fault characteristics. Over a range of slopes from 10°–30°, fault heave and spacing decrease with

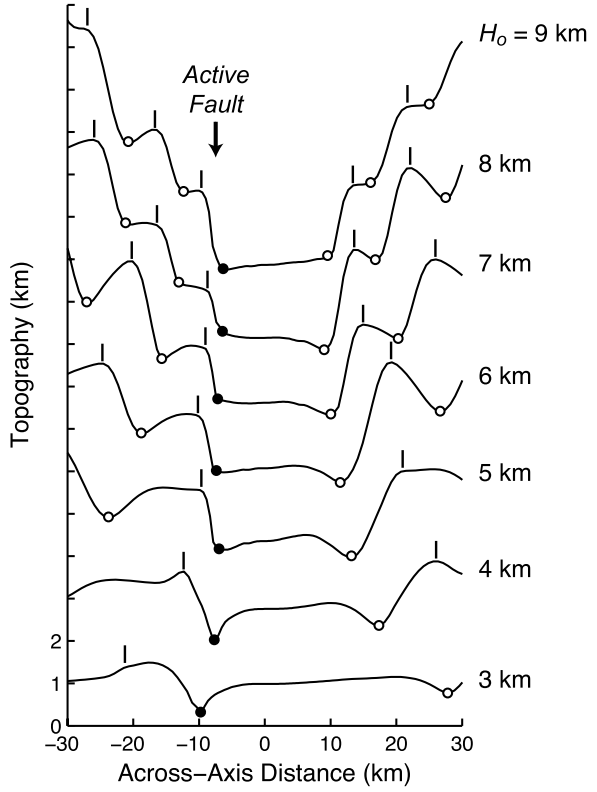

Figure 5. Model topography after 1.5 Ma of spreading for axial lithospheric thicknesses (H_o) ranging from 3 to 9 km and M = 0.7. Small vertical bars and dots show locations of fault tops and bottoms, respectively. Solid dots denote the base of active faults, while open dots show the base of inactive faults. Note that fault heave and spacing increase for thinner axial lithosphere, although total rift relief is greater in thicker lithosphere. Remeshing of the model grid causes topography to smooth sharp corners with time, which introduces an insignificant uncertainty in measurements of fault properties.

increasing slope (Figure 8). These numerical results are consistent with the force-balance model, which predicts that the net force on either side of the active fault (F_F + F_B) will increase with distance away from the axis in proportion to the rate of off-axis, lithosphere thickening. Because (F_F + F_B) increases with lithospheric slope, but F_I remains constant, (F_F + F_B) = F_I at smaller values of x_{AF} and, thus, smaller values of Δx and ΔS.

[18] We next investigated a series of calculations with M = 0.5–1 and H_o = 6 km to quantify the mechanical effects of magma intrusion rate on fault heave and spacing (Figures 6d–6f). These model runs demonstrate that fault heave and spacing increase rapidly with values of M approaching 0.5. In particular, for M < 0.6, a single fault remains stable for the entire length of the model run. The force-balance model provides a good fit to these numerical results, predicting a sharp increase in fault heave and spacing for M < 0.6 due to the $(M - 0.5)^{-1}$ dependence of equations (3) and (4). We next used the force-balance model to extend these results to a wide range of geologically reasonable values for M and H_o (Figure 9). Classifying large-offset faults as those faults for which $\Delta x > H_o$, we find that large-offset faults form where H_o is small and M approaches 0.5 (Figure 9a). Figure 9 also illustrates the sensitivity of fault heave and spacing to the initial cohesion of the brittle layer (C_o) and the critical fault offset required for complete cohesion loss (Δs_c). Specifically, we find that while heave and spacing are relatively insensitive to Δs_c, they both decrease significantly with decreasing values of C_o.

4.2. Thermal Evolution Incorporating Magmatic Heat Input

[19] We next examine a series of simulations in which temperature was allowed to evolve with time. Models were run for half rates appropriate for slow (u_s = 1.0 cm/a) and intermediate (u_s = 2.5 cm/a) spreading ridges, Nusselt numbers of 4 and 8, and values of M between 0.5 and 1. As in the cases with fixed thermal structure, active faults alternate between sides of the ridge axis. The overall axial thermal structure is dominantly controlled by spreading rate, with the rate of magma injection and the efficiency of hydrothermal circulation influencing temperature to a lesser degree (Figure 10). In general, the depths of the 600°C and 1100°C isotherms beneath the ridge axis decrease with increasing M.

[20] Fault growth also influences axial temperatures, creating an asymmetric thermal structure across the ridge axis. Specifically, elevated temperatures are predicted near the base of the lithosphere on side of the ridge axis where the active fault is located. This asymmetry results from the advection of warm mantle material into the footwall of the active fault (Figure 11). After a new fault forms on the opposite side of the ridge axis the thermal perturbation is advected off-axis and gradually decays by diffusion (Figure 11g). The asymmetry is most extreme in the case of long-lived faults (e.g., M = 0.5 shown in Figures 11a–11d) because the axial thermal structure has sufficient time to fully equilibrate with the steady fault geometry. Asymmetry is more subtle, but still present, at higher M values when fault size and spacing are small (e.g., M = 0.8 in Figures 11e and 11f).

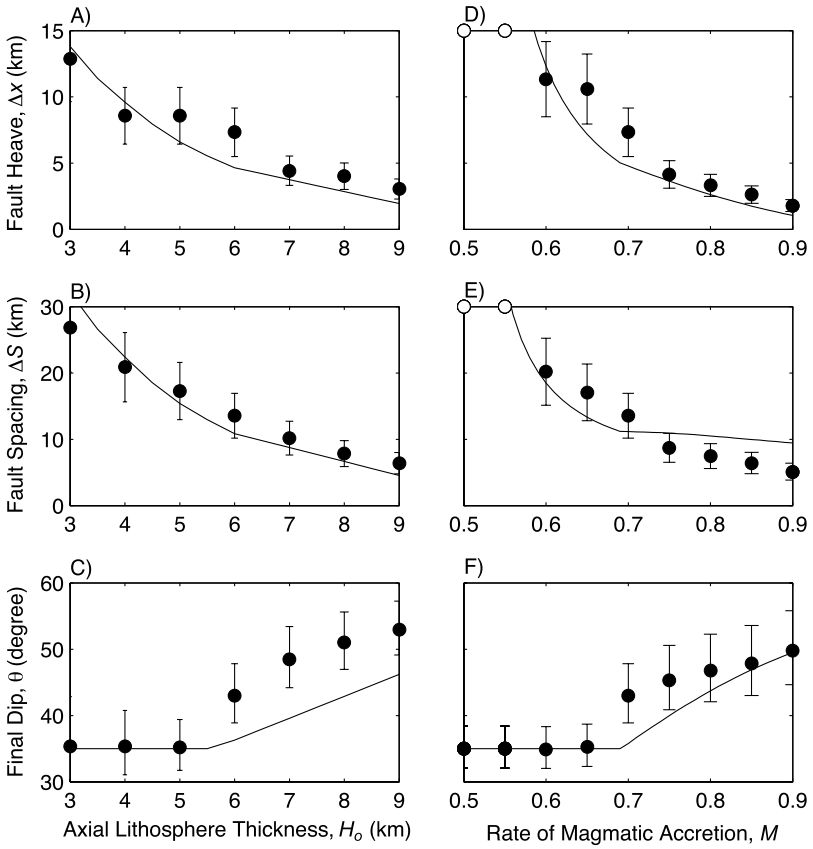

Figure 6. Total fault heave (Δx), fault spacing (ΔS), and final dip angle (θ) versus (a–c) axial lithospheric thickness (H_o) and (d–f) the rate of magmatic accretion (M). Models shown in Figures 6a–6c are calculated for M = 0.7. Models in Figures 6d–6f assume H_o = 6 km. Filled symbols represent the average values of each parameter estimated from all faults formed during a single model run. Open symbols in Figures 6d and 6e indicate model runs with Δx and ΔS that are greater than the vertical axis. Error bars represent ±25% uncertainty on estimates of Δx and ΔS, which is typically sufficient to encompass the variability between individual faults in a model run. Error bars on θ are based on uncertainty in determining dip angle due to the finite width of the fault zone (~3–4 grid elements) in the numerical experiments. Solid curves show predictions from the force-balance model (see Appendix B). Fault dip is calculated assuming an initial dip of 55°, a rotation rate of $d\theta/d\Delta x$ = 5°/km, and a minimum dip of 35°.

[21] Like the results of our runs with imposed thermal structure, these calculations also show that fault heave and spacing are primarily controlled by M, with values of M approaching 0.5 producing larger and more widely spaced faults (Figure 12). The importance of lithospheric structure is secondary, but still evident by comparing fault heave and spacing at the same M but at different spreading rates. Intriguingly, the slow spreading runs (u_s = 1 cm/a) with larger H_0 (as inferred from depth of the 600°C isotherm) produce larger faults than do the intermediate spreading cases (u_s = 2.5 cm/a) with smaller H_0 (Figure 12a). This trend is opposite to what was observed in the fixed thermal structure runs, where thicker axial lithosphere produces smaller, more closely spaced faults (e.g., Figures 6a and 6b).

[22] The more important factor, therefore, appears to be the rate of off-axis lithospheric thickening. Figure 10c shows the lithospheric slope near the ridge axis as calculated from the change in depth of the 600°C isotherm from the axis to a point 5 km off-axis. Cases with u_s = 1 cm/a display a significantly shallower slope than those for u_s = 2.5 cm/a (the smaller u_s creates a larger H_0 and thus less subsequent lithospheric thickening off-axis). This effect is enhanced for values of M approaching 0.5 and in runs with efficient hydrothermal cooling (e.g., Nu = 8). The importance of lithospheric slope is illustrated by comparing a force-balance calculation for H_o = 2 km and ϕ_{lith} = 30° to a calculation with H_o = 6 km and ϕ_{lith} = 15° (Figure 12). Specifically, the later case with a shallower slope predicts larger values of fault heave and spacing for

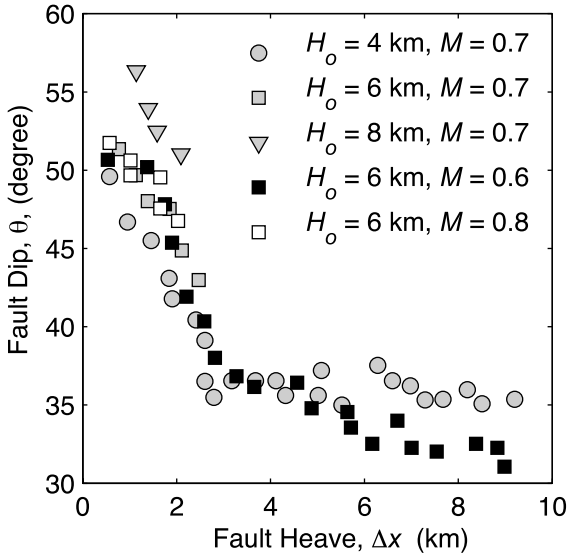

Figure 7. Evolution of fault dip as a function of fault heave for a series of model runs with a fixed axial thermal structure and H_o = 4–8 km and M = 0.6–0.8. For all cases, faults initiate with dips of ~55° consistent with Mohr-Coulomb theory and rotate to a minimum dip angle of 30–35° over ~4 km of fault heave.

M = 0.5–1, even though the axial lithospheric thickness is greater.

[23] In light of this result, the previously noted asymmetry in lithospheric slope associated with faulting could be yet another important factor controlling fault behavior. Our numerical calculations suggest that the relative difference in lithospheric thickness across the ridge axis becomes greater for lower values of M and for slower spreading rates. For the cases in which $M \leq 0.6$ and u_s = 1 cm/a, this asymmetry becomes sufficiently large that it tends to promote faulting on only one side of the axis, i.e., the side with thinner lithosphere. This asymmetry has two effects on the predicted fault characteristics. The first is to complicate the scaling between fault heave and spacing, which is largely controlled by the behavior, at larger M and u_s, of sequential faults forming on opposite sides of the lithosphere. Specifically, for $M \leq 0.6$ and u_s = 1 cm/a, ΔS is smaller for a given Δx than is predicted for cases with faulting on alternating plates. The second effect is to further enhance the lithosphere asymmetry, thereby further stabilizing long-lived normal faults.

5. Discussion

[24] Our numerical models display a style of sequential faulting (e.g., Figure 2) that is consistent with observed seismicity at the Mid-Atlantic Ridge, which shows that active deformation effectively ceases once a fault migrates off-axis beyond the crest of the rift valley [*Smith et al.*, 2003]. We find that total fault heave (Δx) and spacing (ΔS) tend to increase for decreasing values of axial lithospheric thickness (H_o) as predicted by *Buck* [1993], but opposite to the positive relationship inferred from geologic and geophysical observations at mid-ocean ridges [e.g., *Shaw*, 1992; *Malinverno and Cowie*, 1993; *Shaw and Lin*, 1993, 1996]. It thus appears that the more important influence of lithospheric structure on faulting, is the increase in Δx and ΔS with decreasing lithospheric slope. However, the primary control on fault development is the fraction of plate motion accommodated by magmatic accretion (M). Both fault heave and spacing depend nonlinearly on M, because the rate that an active fault migrates into thicker and stronger lithosphere off-axis is proportional to (M − 0.5). Thus, as M approaches 0.5 faults can be nearly stationary and stable for vary long times [*Buck et al.*, 2005].

[25] If correct, this interpretation suggests that intrasegment variations in fault heave and spacing at slow spreading ridge are primarily caused by the mechanical, and secondarily by the thermal, effects

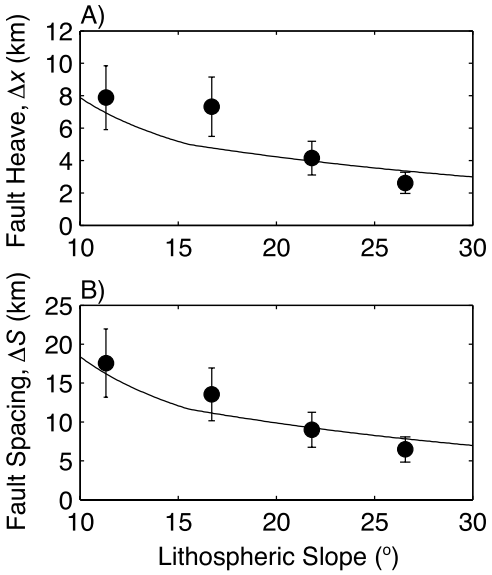

Figure 8. Total (a) fault heave (Δx) and (b) fault spacing (ΔS) as a function of lithospheric slope for H_o = 6 km and M = 0.7. Filled circles represent the average values of each parameter estimated from all faults formed during a single model run with error bars calculated as in Figure 6. Solid curves show predictions from the force-balance model (see Appendix B).

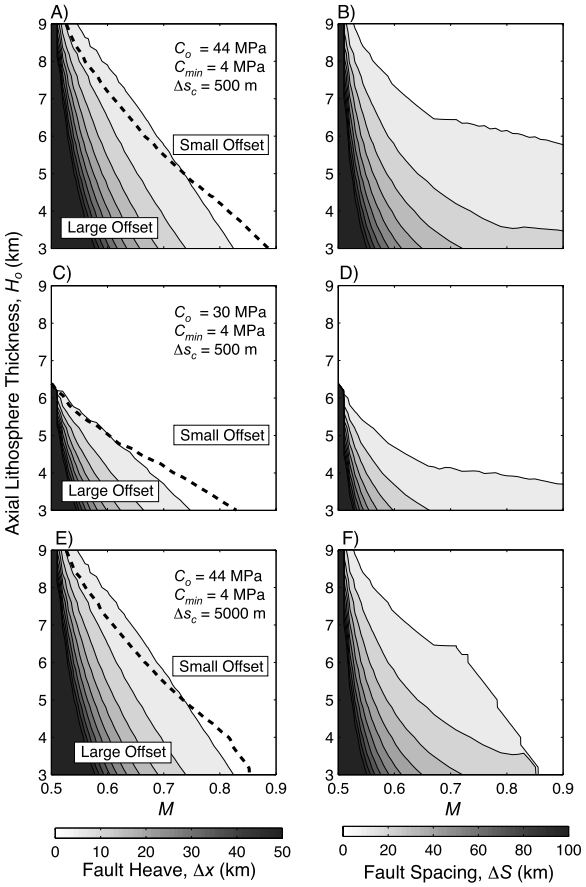

Figure 9. Total fault heave and spacing calculated from the force-balance model (Appendix B) as a function of axial lithospheric thickness and magma accretion rate, M. Results are shown for (a and b) C_o = 44 MPa, $C_{\min}$ = 4 MPa, and Δs_c = 500 m; (c and d) C_o = 30 MPa, $C_{\min}$ = 4 MPa, and Δs_c = 500 m; and (e and f) C_o = 44 MPa, $C_{\min}$ = 4 MPa, and Δs_c = 5000 m. Dashed line denotes boundary between large and small offset faults, where large offset faults are characterized by $\Delta x > H_o$. In general, fault heave and spacing are more sensitive to M than to axial lithospheric thickness.

of reduced magmatic accretion near segment ends. Reduced magma supply at segment ends is consistent with concepts of a high flux of melt being delivered from the mantle to the segment center, redistributed at shallow depths by along-axis dike propagation, and approaching the distal segment ends with reduced frequency [e.g., *Fialko and Rubin*, 1998].

5.1. Comparison to Observations at Slow and Intermediate Spreading Ridges

[26] To test the hypothesis that fault style is controlled by the rate of magma injection at mid-ocean ridges, we used bathymetric data from a range of slow and intermediate spreading ridges to estimate fault heave, fault spacing, and M. Fault heave and spacing were calculated from the average value of each quantity measured from individual across-axis bathymetry profiles (Figure 13). M was estimated by plotting cumulative fault heave as a function of distance off-axis and finding the best fit linear slope to this distribution [*Escartín et al.*, 1999]. For most of the ridges we studied, M ranges from ~0.7–0.85, consistent with previous estimates

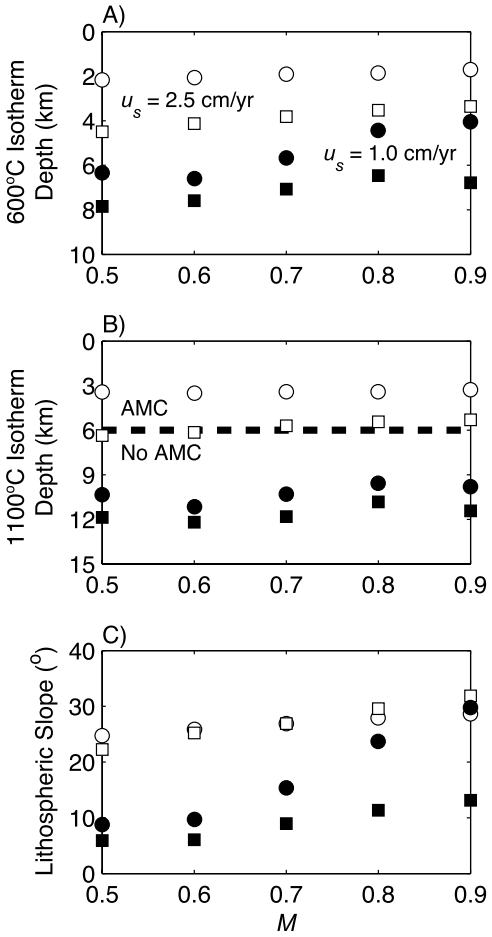

Figure 10. Depth of the (a) 600°C and (b) 1100°C isotherms as a function of magmatic accretion rate, M. (c) Slope of axial lithosphere calculated from the change in depth of the 600°C isotherm from the ridge axis to a point located 5 km off-axis. Filled and open symbols show results for slow (u_s = 1.0 cm/a) and intermediate (u_s = 2.5 cm/a) spreading rates, respectively. Circles and squares denote Nusselt numbers of 4 and 8, respectively. Dashed line in Figure 10b illustrates threshold depth at which an axial magma chamber (AMC) would be predicted to form within a 6-km thick crust on the basis of the depth of the 1100°C isotherm.

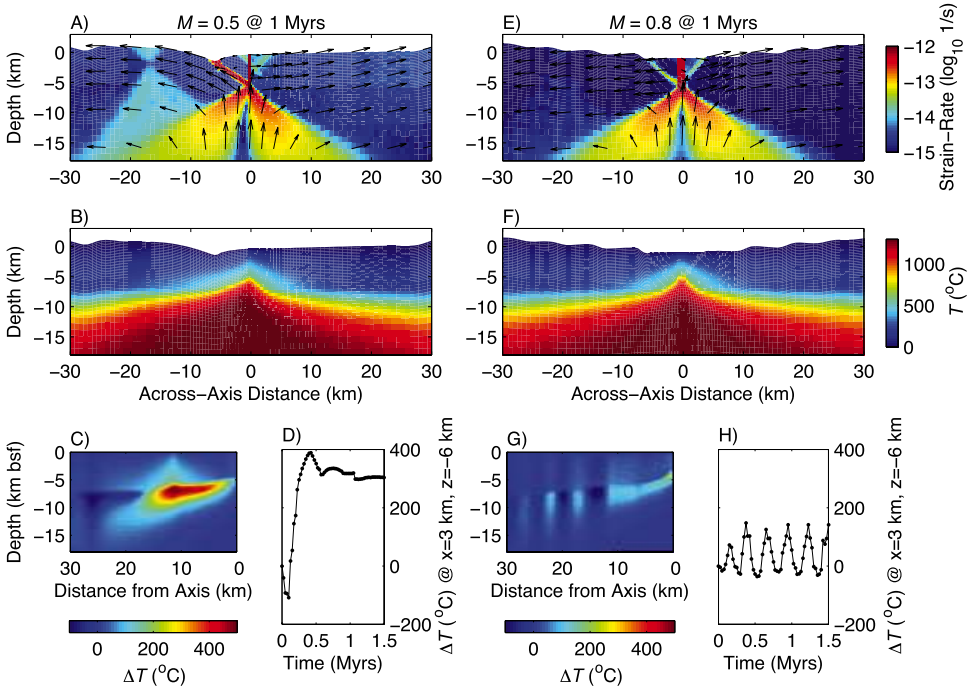

Figure 11. Model runs showing deformation and thermal structure after 0.95 Ma of extension for (a–d) $M = 0.5$ and (e–h) $M = 0.8$ assuming $u_s = 2.5$ cm/a and $Nu = 8$. Illustrated are (a and e) strain rate, (b and f) temperature, (c and g) temperature difference, ΔT, between the two sides of the ridge axis at a given distance from the axis and depth beneath the seafloor, and (d and h) ΔT as a function of time at a point located 3 km off-axis and at a depth of 6 km. ΔT is greater in the case of $M = 0.5$ because the thermal structure equilibrates with the large-offset fault that forms on the left side of the ridge axis. In contrast, the small-offset faults formed in the $M = 0.8$ remain cooler and fluctuate as faulting alternates sides of the ridge axis.

from cumulative fault throw [*Escartín et al.*, 1999] and seismic moment release [*Solomon et al.*, 1988] at slow spreading ridges. However, several profiles from the Mid-Atlantic Ridge displayed M values of 0.4–0.6. These locations typically correspond to the end of spreading segments and coincide with previously identified oceanic core complexes (e.g., Kane megamullion at 23.5°N MAR [*Tucholke et al.*, 1998] shown in Figure 13d).

[27] In general, these data show that fault heave and spacing increase as M decreases toward 0.5 in agreement with the trends predicted by the force-balance model and our numerical simulations (Figure 14). We find that the data can be best fit with a maximum cohesion of 30 MPa and lithospheric slopes ranging from 10° to 30°, consistent with the slopes predicted by our thermal models (Figure 10c). The observed values of fault heave are slightly smaller than predicted by the force-balance model at values of M approaching 0.5. Estimates of heave and spacing in regions of low M are sensitive to additional processes not included in the force-balance model. For example, the model does not account for flexural faulting in the footwall of an oceanic core complex. Small faults associated with unbending of the footwall will reduce average fault heave, spacing, as well as estimates of M from bathymetric data (e.g., see MAR profiles in Figure 13d), thus biasing the direct comparison of the mid-ocean ridge data with the force-balance model. However, the general inverse relationship between fault heave and spacing and values of M between 0.5 and 1 (Figure 14) supports our assertion that fault style is strongly controlled by the rate of magmatic accretion at mid-ocean ridges.

5.2. Role of Magmatism in the Evolution of Oceanic Core Complexes

[28] Large-offset normal faults are an important class of faults at mid-ocean ridges because of their potential to exhume lower crustal and upper mantle rocks at the seafloor in oceanic core complexes [*Karson and Dick*, 1983; *Cannat*, 1993; *Tucholke and Lin*, 1994; *Cann et al.*, 1997; *Tucholke et al.*, 1998]. Several competing models have been proposed regarding the role of magmatism in the

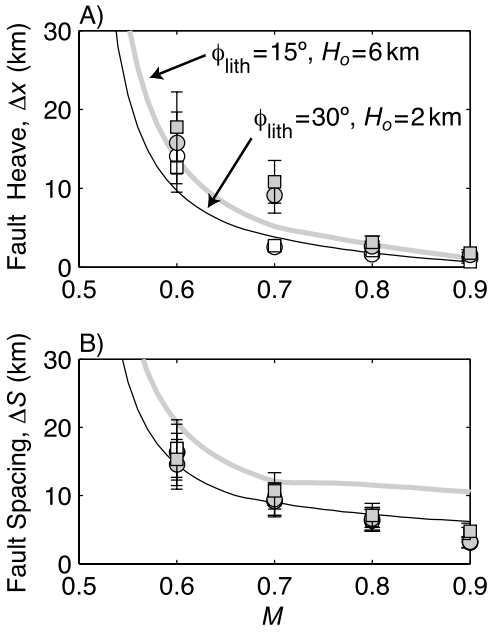

Figure 12. (a) Total fault heave and (b) fault spacing as a function of M for models with thermal evolution. Gray and white symbols show results for slow (u_s = 1.0 cm/a) and intermediate (u_s = 2.5 cm/a) spreading rates, respectively. Squares and circles denote Nusselt numbers of 4 and 8, respectively. Error bars are calculated as in Figure 6. Solid and gray lines show predictions from the force-balance model (Appendix B) assuming H_o = 2 km, ϕ_{lith} = 30° and H_o = 6 km, ϕ_{lith} = 15°, respectively.

formation of oceanic core complexes. *Tucholke and Lin* [1994] proposed that core complexes form during periods of amagmatic spreading and are terminated by later magmatic periods. In this model, the core complex (or megmamullion) is created by a long-lived detachment fault that cuts the entire lithosphere and soles near the brittle-ductile transition [*Tucholke et al.*, 1998, 2001]. Dredging [*Karson and Dick*, 1983; *Cannat*, 1993; *Cannat et al.*, 1995, 1997; *Blackman et al.*, 1998; *Escartín et al.*, 2003] and residual gravity anomalies [*Tucholke and Lin*, 1994; *Tucholke et al.*, 1997; *Blackman et al.*, 1998] indicate that gabbros and serpentinized peridotites are exposed in the fault footwall, leading to the suggestion that deformation on the detachment is localized by the presence of serpentine [*Cann et al.*, 1997; *Escartín et al.*, 1997; *Tucholke et al.*, 1998].

[29] An alternative model has been proposed by *Dick et al.* [1991, 2000], who argue that core complexes form during magmatic periods and that the detachment soles into a melt-rich region in the shallow lithosphere located near the dike-gabbro transition. This model is supported by evidence for melt-assisted deformation in fault rocks sampled from Hole 735B on Atlantis Bank (57°17′E Southwest Indian Ridge) [*Dick et al.*, 2000; *Natland and Dick*, 2001]. However, in contrast most footwall rocks exposed in core complexes on the Mid-Atlantic Ridge show no evidence for high-temperature deformation [*Escartín et al.*, 2003], suggesting a much cooler thermal regime during fault formation than proposed by *Dick et al.* [2000]. *Ildefonse et al.* [2007] proposed a hybrid model for core complex formation, in which the detachment is initiated by the rheologic contrast between gabbroic intrusions and surrounding peridotite. In this scenario, core complex formation is associated with mafic intrusions, but does not require active faulting in the presence of melt.

[30] More recently, *Buck et al.* [2005] proposed that oceanic core complexes form at intermediate rates of magmatism, when the accretion accommodates ~50% of the total plate separation rate. This model is supported by geologic and geophysical observations that indicate megamullion frequency along mid-ocean ridges correlates with intermediate rates of magmatism. *Tucholke et al.* [2008] used residual gravity anomalies to show that some detachment terminations correspond to periods of crustal thickening, while others correspond to crustal thinning. On the basis of these observations, *Tucholke et al.* [2008] concluded that oceanic core complexes form under restricted conditions when the rate of magmatism is neither too high nor too low (the "Goldilocks hypothesis").

[31] Our results showing increased fault throw and heave as M approaches 0.5 support the "Goldilocks hypothesis" for the formation of core complexes. In addition, our numerical results suggest that depending on the spreading rate and efficiency of hydrothermal circulation, core complexes can form in either the presence (e.g., u_s = 2.5 cm/a, Nu = 4) or absence (u_s = 1.0 cm/a, Nu = 4) of a crustal magma chamber (Figure 10). In our models, the key for generating large offset faults is the rate of accretion in the brittle portion of the lithosphere. Thus, so long as ~50% of the extension above the brittle-ductile transition is supported by magmatism a large-offset fault is predicted to form. This result may help to explain the apparently discrepant temperature conditions recorded in fault rocks from different detachments, and implies that a one-size-fits-all thermal model is not necessary for all oceanic core complexes.

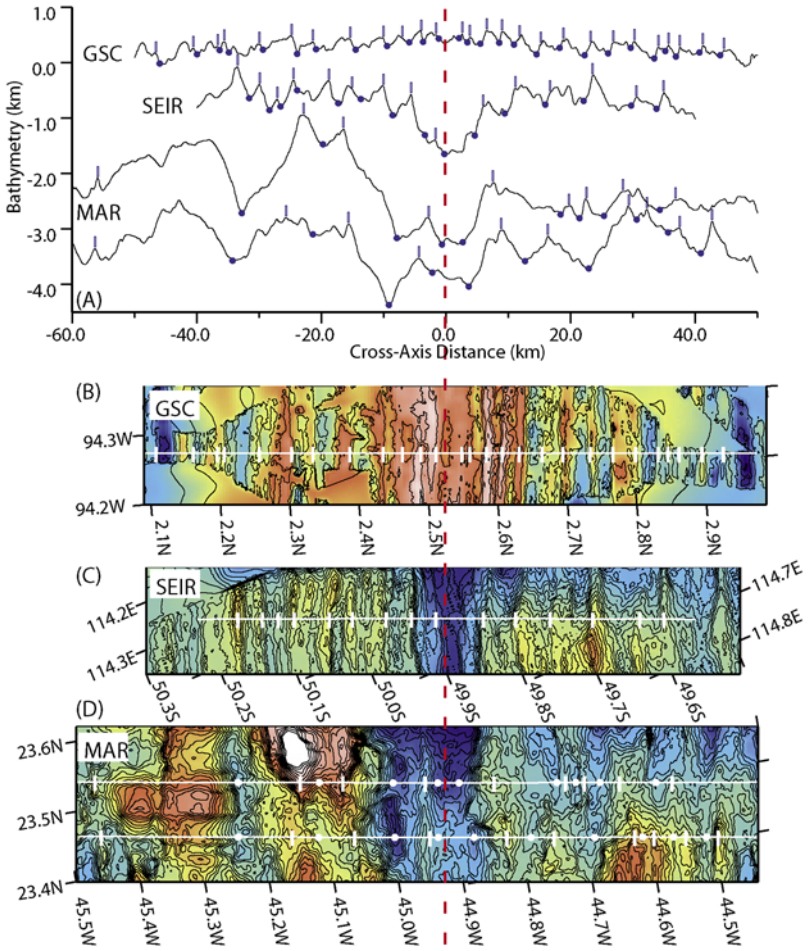

Figure 13. (a) Example bathymetry profiles across the Galapagos Spreading Center (GSC), Southeast Indian Ridge (SEIR), and Mid-Atlantic Ridge (MAR). Oblique Mercator projections of multibeam bathymetry show the locations of the above profiles across the (b) GSC, (c) SEIR, and (d) MAR. Long vertical (red) dashed line marks our picks of the approximate center of the axes. Small vertical bars and dots mark our picks of fault tops and bottoms (not shown in Figures 13b–13c), respectively. West of the MAR, bars mark breakaway locations, and the solid circles mark terminations of oceanic core-complex identified by *Tucholke et al.* [1998].

[32] Lithospheric structure may also play a secondary role on the longevity of oceanic detachment faults. The reduced rate of off-axis lithospheric thickening beneath the active fault will tend to stabilize the active fault by making it more difficult to initiate a fault in the thicker lithosphere on the opposite side of the ridge axis. In situations where the asymmetry is extreme (e.g., cases with low u_s and M approaching 0.5), it may also result in the breakdown of the sequential fault model, focusing deformation onto one side of the ridge axis for multiple fault cycles.

5.3. Fault Controls on Hydrothermal Venting

[33] The two primary mechanisms proposed for promoting high-temperature hydrothermal venting are the heat supplied by crustal magma chambers [*Cann et al.*, 1985] and cracking fronts into hot, but unmelted rock [*Lister*, 1974; *Wilcock and Delaney*, 1996]. The coincidence of high-temperature vent sites above seismically identified crustal magma chambers [e.g., *Detrick et al.*, 1987; *Singh et al.*, 1998, 2006; *Martinez et al.*, 2006; *Van Ark et al.*, 2007] supports cooling and crystallization of basaltic melts as the heat source for volcanically hosted hydrothermal systems at magmatically robust ridges [e.g., *Cannat et al.*, 2004]. In contrast, tectonically hosted vent systems typically form at slow spreading, magma poor ridges, and sometimes in the absence of a crustal magma chamber. Modeling suggests that if cracking fronts extend deep enough into hot (but unmelted) lithosphere, they can supply sufficient heat to drive these hydrothermal [*Cannat et al.*, 2004; *German and*

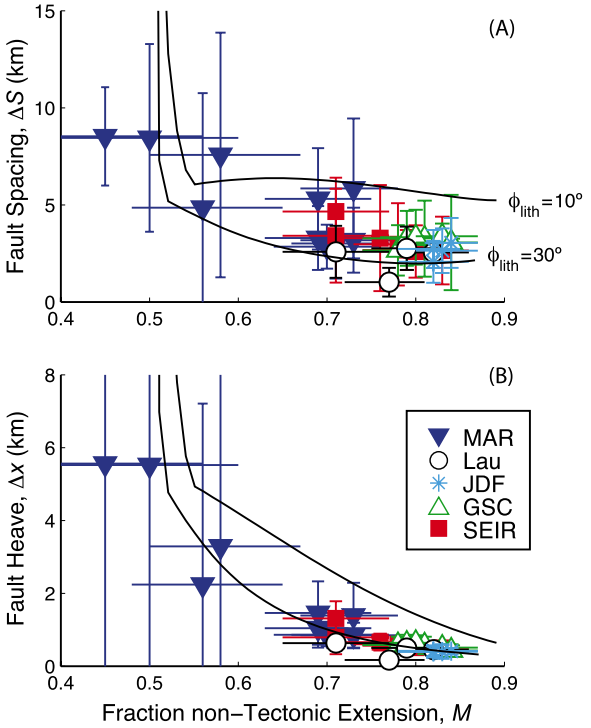

Figure 14. (a) Average fault spacing and (b) heave versus fraction nontectonic strain, M, as estimated from our picks of fault tops and bottoms along the GSC, SEIR, MAR, Lau Basin (Lau), and Juan de Fuca Ridge (JDF). M is estimated from the best fitting slope of cumulative fault heave versus distance on both sides of the axis. Errors in M are based on an estimate of 20% error in this slope. Errors in spacing and heave are ± one standard deviation of the population for each profile. Theoretical predictions are calculated from the force-balance model (Appendix B) assuming lithospheric slopes of 10° and 30°. Calculations assume an axial lithospheric thickness H_o = 6 km, a fault rotation rate of $d\theta/d\Delta x$ = 5°/km, a minimum fault dip of 35°, and an initial and minimum cohesion of 30 and 4 MPa, respectively. Kinks in curves at M ∼ 0.55 correspond to situations in which large offset faults rotate to the minimum dip angle before a new fault is formed. In these cases, θ no longer evolves with fault heave in equation (B2), resulting in the change in curvature of the theoretical predictions.

Lin, 2004]. These theoretical studies are supported by recent seismic data from the TAG segment of the Mid-Atlantic ridge, which shows no evidence for crustal melt beneath the TAG hydrothermal mound [*Canales et al.*, 2007].

[34] The TAG mound sits directly above a low-angle normal fault, which has been interpret to represent the early stages of formation of an oceanic core complex [*Canales et al.*, 2007; *deMartin et al.*, 2007]. Thus, its location corresponds to the region of elevated temperatures in the footwalls of the large-offset faults produced in our M = 0.5–0.6 models (e.g., Figures 11b and 11c). Moreover, tectonically hosted, high-temperature vent sites and deposits associated with ultramafic lithologies (suggesting significant unroofing on normal faults) have been identified at Rainbow and Logachev vent fields on the Mid-Atlantic Ridge [*Cherkashev et al.*, 2000; *Charlou et al.*, 2002] and along the Knipovich [*Connelly et al.*, 2007] and Southwest Indian Ridge [*German et al.*, 1998; *Bach et al.*, 2002]. Taken together these observations suggest that the upward advection of heat due to exhumation of the footwall on long-lived normal faults combined with increased permeability in the active fault zone may play an important role in focusing tectonically hosted hydrothermal systems. Future modeling studies that fully couple crustal deformation with fluid circulation are necessary to better constrain the feedbacks between hydrothermal circulation, alteration, and detachment faulting.

6. Conclusions

[35] Using numerical models we have shown that faulting at mid-ocean ridges typically follows a sequential pattern of initiation, growth, and termination. Under all conditions examined in this study a single active fault initiates near the ridge axis and is subsequently rafted off-axis by continued magmatic accretion, until it becomes mechanically easier to break a new fault than continue deforming on the original fault. This new fault forms on the opposite side of the ridge axis from the existing fault, where tensile stresses are highest. As this process continues through time it generates seafloor morphology similar to the abyssal hill topography seen at many slow and intermediate spreading ridges.

[36] Faulting is influenced by a number of competing factors including lithospheric structure, rheology, and the rate of magma accretion at the ridge axis. In agreement with previous studies of the mechanics of faulting and contrary to qualitative inferences, we find that fault heave and spacing decrease with increasing lithospheric thickness. We also find that fault heave and spacing increase with decreasing rate of off-axis lithosphere thickening. However, what appears to be the dominant factor controlling fault growth is the ratio of magmatic accretion to the rate far field extension (M), with the largest, most widely spaced faults occurring for

values of M decreasing toward 0.5. Observations from slow and intermediate spreading ridges support the inverse relation between fault heave and spacing with M predicted by our force-balance and numerical calculations.

[37] Our results are consistent with a model in which oceanic core complexes form under intermediate rates of magma accretion [*Buck et al.*, 2005; *Tucholke et al.*, 2008]. Furthermore, fault growth generates a strongly asymmetric axial thermal structure, with elevated temperatures at the base of the lithosphere below the active fault. This asymmetry results from the advection of warm mantle material into the footwall of the active fault and is most pronounced for long-lived, large-offset normal faults. These across-axis variations in thermal structure will further stabilize slip on large-offset normal faults and offer a plausible mechanism for localizing hydrothermal circulation on the footwall of oceanic core complexes.

Appendix A: Model Description

A1. Conservation of Mass and Momentum

[38] The FLAC method employs an implicit time-marching scheme to solve for conservation of mass [*Cundall*, 1989]

$$\frac{\partial v_i}{\partial x_i} = 0 \tag{A1}$$

and momentum

$$\rho \frac{Dv_i}{Dt} = \frac{\partial \sigma_{ij}}{\partial x_j} + \rho g \tag{A2}$$

where v_i is the nodal velocity in the x_i direction, ρ is density, g is the gravitational acceleration, σ_{ij} is the stress tensor, and $\frac{D}{Dt}$ denotes the material time derivative. The nodal accelerations (left-hand side of equation (A2)) are integrated in time to give updated nodal velocities, strains and strain rates. Using the constitutive laws the strains and strain rates are used to calculate new elastic and viscous stresses, respectively (right-hand side of equation (A2)). Finally, these stresses are used to determine the accelerations for the next time step.

[39] The length of the time step is the minimum of the Maxwell relaxation time ($2\eta/E$) and the time required for an elastic P wave to propagate across the local grid spacing. Because of the high grid resolution ($\sim$0.25 km) used in our calculations, the elastic propagation time would result in extremely short time steps and large computational times. To circumvent this problem we employ the adaptive density scaling method of *Cundall* [1982]. This approach assumes that when the inertial term in equation (A2) is small, the density on the left-hand side of equation (A2) (i.e., the inertial density) and hence the time step can be increased. Following *Lavier et al.* [2000] we chose a ratio for the imposed boundary velocity to the P wave velocity (reduced by increasing inertial density) of 5×10^{-5}, resulting in a time step of 1–5 years.

[40] The computation mesh consists of quadrilateral elements that are subdivided into 4 triangular subelements. The final solution in each quadrilateral element is the average of the solution in the 4 triangular subelements. Because the FLAC method is Lagrangian, large deformations result in highly a distorted numerical grid, which decreases numerical accuracy. We account for this problem by remeshing the model space when the minimum angle in any triangular element decreases below 5°. During remeshing strains are interpolated from the old (deformed) to the new (undeformed) grid by linear interpolation [*Lavier and Buck*, 2002]. This interpolation results in artificial accelerations that decay over several hundred time steps. To reduce the model time during which these artificial accelerations influence solutions (thus minimizing their total influence in a time-integrated sense), we decrease the time step by an order of magnitude immediately following a remeshing event and then increase it linearly to its original value over 1000 time steps.

A2. Solution of the Energy Equation for Magma Intrusion

[41] To calculate temperature we solve the energy equation accounting for the heat added via magma emplacement and crystallization within the injection zone

$$\frac{DI}{Dt} = \left(\frac{\partial I}{\partial m_L}\right)_{m_c} \frac{Dm_L}{Dt} + \left(\frac{\partial I}{\partial m_C}\right)_{m_L} \frac{Dm_C}{Dt} + \frac{\nabla \cdot q}{\rho} \tag{A3}$$

Here I is the specific internal heat (i.e., $I = C_pT$), C_p is the specific heat, m_L is the mass of the added magma, m_C is the crystal mass, q is the diffusive heat flow, and ρ is density. The first term on the right-hand side of equation (A3) represents the heat carried by the injected liquid magma,

$$\left(\frac{\partial I}{\partial m_L}\right)_{m_c} \frac{Dm_L}{Dt} = C_p\left(T_{liq} - T\right)\frac{u_{dike}}{x_{inj}} \tag{A4}$$

where T_{liq} is the liquidus temperature, u_{dike} is the injection rate, and x_{inj} is the width of the injection zone. The second term on the right hand side of equation (A3) accounts for the heat released by generating crystals. The first part is

$$\left(\frac{\partial I}{\partial m_C}\right)_{m_L} = L/m \tag{A5}$$

where L is the latent heat released per kg of melt crystallized and m represents the mass of the infinitesimal control volume. The change in crystal mass has two parts,

$$\frac{Dm_C}{Dt} = \left(\frac{\partial m_C}{\partial t}\right)_m \frac{DT}{Dt} + \left(\frac{\partial m_C}{\partial m}\right)_T \frac{Dm}{Dt}. \tag{A6}$$

The first part represents the change in crystallinity with changes in the local temperature T and the second part represents the new crystal mass forming out of the injected mass as it (instantaneously) equilibrates to the local temperature.

$$\frac{Dm_C}{Dt} = \begin{cases} 0 & \left(T \geq T_{liq};\ \ F_C = \dfrac{m_c}{m} = 0\right) \\ \dfrac{-m}{T_{liq} - T_{sol}} \dfrac{DT}{Dt} + m\left(\dfrac{T_{liq} - T}{T_{liq} - T_{sol}}\right) \dfrac{u_{dike}}{x_{inj}} & \left(T_{liq} > T \geq T_{sol};\ \ 0 \leq \dfrac{m_c}{m} \leq 1\right) \\ 0 + m\dfrac{u_{dike}}{x_{inj}} & \left(T \leq T_{sol};\ \ F_C = \dfrac{m_c}{m} = 1\right) \end{cases} \tag{A7}$$

where F_c is the fraction of crystallinity approximated to be a linear function of temperature between the liquidus (T_{liq}) and solidus (T_{sol}). Combining equations (A3), (A4), and (A7) results in the following heat equation

$$\frac{DT}{Dt} = \begin{cases} \nabla \cdot (\kappa \nabla T) & \left(T \geq T_{liq}\right) \\ \nabla \cdot \left[\dfrac{\kappa}{\left(1 + \dfrac{L}{C_P\left(T_{liq} - T_{sol}\right)}\right)} \nabla T\right] + \left(T_{liq} - T\right)\dfrac{u_{dike}}{x_{inj}} & \left(T_{liq} > T \geq T_{sol}\right) \\ \nabla \cdot (\kappa \nabla T) + \left[\left(T_{liq} - T\right) + \dfrac{L}{C_p}\right]\dfrac{u_{dike}}{x_{inj}} & \left(T \leq T_{sol}\right) \end{cases} \tag{A8}$$

Note equation (A8) is the heat diffusion equation with a source (equation (2)). The first term represents diffusion with a modified thermal diffusivity. Diffusivity is further modified to incorporate the effects of hydrothermal circulation by increasing κ by a factor, Nu, in regions of the model space above a depth of 7 km and where $T <$ 600°C [e.g., *Phipps Morgan et al.*, 1987]. The threshold depth is an approximation for the maximum pressure at which cracks are predicted to remain open for hydrothermal circulation, and the cut-off temperature is consistent with the maximum alteration temperature observed in rocks from the lower oceanic crust [*Gillis et al.*, 1993].

[42] Numerically we implement the source term in equation (A8) by adjusting the temperature in the injection zone at each time step, k, by

$$T = T_{k-1} + \varepsilon_{xx}^{dike}\left(T_{liq} - T_{k-1}\right) \tag{A9}$$

where T_{k-1} is the temperature at the previous time step, and ε_{xx}^{dike} is the increment of horizontal strain across the injection zone imposed at the time step.

A3. Rheology

[43] In our model, material behavior is a function of the thermal structure, stress, and accumulated plastic strain throughout the model space [*Poliakov and Buck*, 1998; *Lavier et al.*, 2000]. In regions where deformation is visco-elastic, the material behaves as a Maxwell solid in which the deviatoric stresses, σ^{dev}, are related to the deviatoric strains, ε^{dev}, by

$$\dot{\varepsilon}_{ij}^{dev} = \frac{1}{2\eta}\sigma_{ij}^{dev} + \frac{1}{E}\dot{\sigma}_{ij}^{dev} \tag{A10}$$

where E is Young's modulus, η is the effective viscosity, and dotted quantities represent derivatives with respect to time. The isotropic part of the

deformation field is assumed to be purely elastic, with the isotropic stress and strain related by

$$\varepsilon_{ii} = \frac{1}{3K}\sigma_{ii} \tag{A11}$$

where K is the bulk modulus. Viscous deformation is incompressible and follows a non-Newtonian temperature and strain rate dependent power law of the form [*Kirby*, 1983; *Chen and Morgan*, 1990; *Kohlstedt et al.*, 1995]

$$\eta = \frac{1}{4}\left(\frac{4}{3A}\right)^{1/n}\dot{\varepsilon}_{II}^{(1/n)-1}\exp\left(\frac{Q}{nRT}\right) \tag{A12}$$

in which A is a material constant, n is the power law exponent, $\dot{\varepsilon}_{II}$ is the second invariant of the strain rate tensor, Q is the activation energy, and R is the universal gas constant.

[44] Plastic yielding in the brittle layer is controlled by Mohr-Coulomb theory [*Poliakov and Buck*, 1998]. The failure criteria is given by [*Jaeger and Cook*, 1979]

$$\tau = \mu\sigma_n + C \tag{A13}$$

where τ is the shear stress required for faulting, μ is the coefficient of friction, σ_n is the normal stress, and C is the cohesion. Because σ_n is dominated by the lithostatic stress, τ increases linearly with depth. Following *Poliakov and Buck* [1998], we simulate the weakening of brittle materials after failure by using a strain-dependent cohesion law. The initial cohesion, C_o, decreases linearly with the total accumulated plastic strain until it reaches a minimum value, C_{min}, after a critical increment of plastic strain of ε_c. For a characteristic fault zone width, Δd, the strain required for complete cohesion loss can be interpreted in terms of a critical fault offset, $\Delta s_c = \varepsilon_c \Delta d$ [*Lavier et al.*, 2000]. In general, Δd is 2–4 times the grid resolution, therefore for a grid resolution of 250 m and $\varepsilon_c = 0.5$ we find $\Delta s_c = 250$–500 m. To reduce the broadening of fault zones due to numerical diffusion caused by regridding (see below) we also include an annealing time in our calculations in which plastic strain decays over 10^{12} s.

Appendix B: Force-Balance Model for Faulting at Mid-Ocean Ridges

[45] Fault evolution is modeled following a force-balance approach [*Forsyth*, 1992; *Buck*, 1993; *Lavier et al.*, 2000], such that a new fault will form when the force required to continue slip on the active fault exceeds the force required to initiate a new fault at the axis:

$$F_F + F_B \geq F_I \tag{B1}$$

Strictly, $F_F + F_B$ represent the depth-integrated, nonlithostatic, tensile stress on the lithosphere on either side of the fault and F_I is the depth-integrated yield strength of the unfaulted (i.e., with full cohesive strength) lithosphere. Following *Forsyth* [1992],

$$F_F = \frac{\mu\rho g H^2/2 + HC(\varepsilon)}{\mu\sin(\theta)^2 + \sin(\theta)\cos(\theta)} \tag{B2}$$

and

$$F_I = \frac{\mu\rho g H_o^2/2 + H_o C_o}{\mu\sin(\theta_o)^2 + \sin(\theta_o)\cos(\theta_o)}. \tag{B3}$$

Force F_F represents the force needed to cause further slip on the fault plane; it is identical in form to F_I, but F_I depends on the initial fault dip (θ_o), cohesion, and axial lithospheric thickness (H_o), whereas F_F depends on the values of these properties as they evolve on the fault as it moves off-axis. Immediately after the initiation of a new fault, F_F decreases as the cohesion on the fault drops with the accumulated plastic strain. However, after fault slip exceeds the critical offset (Δs_c) required for complete cohesion loss, F_F gradually increases owing to the off-axis thickening of the lithosphere (Figure 3).

[46] Following the scaling law for a elastic-plastic layer of *Lavier et al.* [2000],

$$F_B = AH^2(1 - \exp(-B\Delta x'/H)), \tag{B4}$$

where A and B are constants related to the elastic-plastic properties of the lithosphere. Equation (B4) describes the force needed to bend the lithosphere as the fault heave ($\Delta x'$) increases. Equation (B4) includes plastic weakening of the plate with continued bending and therefore predicts a peak in F_B with a maximum value of AH^2 (Figure 3).

[47] By solving equation (B1) for $\Delta x'$ we can determine x_{AF}, and then predict total fault heave (Δx) and fault spacing (ΔS) using equations (3) and (4), respectively. Figure 3 illustrates an example calculation of F_F, F_B, and F_I for $H_o = 6$ km and $M = 0.7$. A new fault is predicted to form when $\Delta x' \sim 5$ km, corresponding to the point at which the active fault has migrated $x_{AF} \sim 3.4$ km

off-axis. Calculating fault spacing from equation (3) implies $\Delta S \sim 12$ km, which is consistent with the numerical results shown in Figure 6b.

Acknowledgments

[48] Funding for this research was provided by NSF grants OCE-0327018 (M.D.B.), OCE-0548672 (M.D.B.), OCE-0327051 (G.I.), and OCE-03-51234 (G.I.). This work has benefited from many fruitful discussions with R. Buck, B. Tucholke, R. Qin, S. Sacks, J. P. Canales, L. Lavier, G. Hirth, J. Lin, and E. Mittelstaedt. We are indebted to A. Poliakov, L. Lavier, and R. Buck for their extensive work in adapting the FLAC code for mid-ocean ridge applications and for generously making this code available to us. Finally, we thank R. Buck and an anonymous reviewer for careful reviews that improved this manuscript. Several figures were produced with GMT 3.4 [*Wessel and Smith*, 1995].

References

Abdallah, A., et al. (1979), Relevance of Afar seismicity and volcanism to the mechanics of accreting plate boundaries, *Nature*, *282*, 17–23, doi:10.1038/282017a0.

Bach, W., N. R. Banerjee, H. J. B. Dick, and E. T. Baker (2002), Discovery of ancient and active hydrothermal systems along the ultra-slow spreading Southwest Indian Ridge 10–16°E, *Geochem. Geophys. Geosyst.*, *3*(7), 1044, doi:10.1029/2001GC000279.

Ballard, R. D., and T. H. van Andel (1977), Morphology and tectonics of the inner rift valley at 36°50′N on the Mid-Atlantic Ridge, *Geol. Soc. Am. Bull.*, *88*, 507–530, doi:10.1130/0016-7606(1977)88<507:MATOTI>2.0.CO;2.

Barclay, A. H., D. R. Toomey, and S. C. Solomon (2001), Microearthquake characteristics and crustal Vp/Vs structure at the Mid-Atlantic Ridge, 35°N, *J. Geophys. Res.*, *106*, 2017–2034, doi:10.1029/2000JB900371.

Behn, M. D., W. R. Buck, and I. S. Sacks (2006), Topographic controls on dike injection in volcanic rift zones, *Earth Planet. Sci. Lett.*, *246*, 188–196, doi:10.1016/j.epsl.2006.04.005.

Behn, M. D., M. S. Boettcher, and G. Hirth (2007), On the thermal structure of oceanic transform faults, *Geology*, *35*, 307–310, doi:10.1130/G23112A.1.

Blacic, T. M., G. Ito, J. P. Canales, R. S. Detrick, and J. Sinton (2004), Constructing the crust along the Galapagos Spreading Center 91.3°–95.5°W: Correlation of seismic layer 2A with axial magma lens and topographic characteristics, *J. Geophys. Res.*, *109*, B10310, doi:10.1029/2004JB003066.

Blackman, D. K., J. R. Cann, B. Janssen, and D. K. Smith (1998), Origin of extensional core complexes: Evidence from the mid-Atlantic ridge Atlantis Fracture Zone, *J. Geophys. Res.*, *103*, 21,315–21,333, doi:10.1029/98JB01756.

Buck, W. R. (1993), Effect of lithospheric thickness on the formation of high- and low-angle normal faults, *Geology*, *21*, 933–936, doi:10.1130/0091-7613(1993)021<0933:EOLTOT>2.3.CO;2.

Buck, W. R., L. L. Lavier, and A. N. B. Poliakov (2005), Modes of faulting at mid-ocean ridges, *Nature*, *434*, 719–723, doi:10.1038/nature03358.

Bull, J. M., et al. (2003), Fault and magmatic interaction within Iceland's western rift over the last 9 kyr, *Geophys. J. Int.*, *154*, F1–F8, doi:10.1046/j.1365-246X.2003.01990.x.

Canales, J. P., J. J. Dañobeitia, R. S. Detrick, E. E. E. Hooft, R. Bartolomé, and D. F. Naar (1997), Variations in axial morphology along the Galápagos spreading center and the influence of the Galápagos hotspot, *J. Geophys. Res.*, *102*(B12), 27,341–27,354, doi:10.1029/97JB01633.

Canales, J. P., R. S. Detrick, J. Lin, J. A. Collins, and D. R. Toomey (2000), Crustal and upper mantle seismic structure beneath the rift mountains and across a nontransform offset at the Mid-Atlantic Ridge (35°N), *J. Geophys. Res.*, *105*, 2699–2719, doi:10.1029/1999JB900379.

Canales, J. P., R. S. Detrick, S. M. Carbotte, G. M. Kent, J. B. Diebold, A. Harding, J. Babcock, M. R. Nedimoviæ, and E. van Ark (2005), Upper crustal structure and axial topography at intermediate spreading ridges: Seismic constraints from the southern Juan de Fuca Ridge, *J. Geophys. Res.*, *110*, B12104, doi:10.1029/2005JB003630.

Canales, J. P., R. A. Sohn, and B. J. deMartin (2007), Crustal structure of the Trans-Atlantic Geotraverse (TAG) segment (Mid-Atlantic Ridge, 26°10′N): Implications for the nature of hydrothermal circulation and detachment faulting at slow spreading ridges, *Geochem. Geophys. Geosyst.*, *8*, Q08004, doi:10.1029/2007GC001629.

Cann, J. R., M. R. Strens, and A. Rice (1985), A simple magma-driven thermal balance model for the formation of volcanogenic massive sulphides, *Earth Planet. Sci. Lett.*, *76*, 123–134, doi:10.1016/0012-821X(85)90153-0.

Cann, J. R., et al. (1997), Corrugated slip surfaces formed at ridge-transform intersections on the Mid-Atlantic Ridge, *Nature*, *385*, 329–332, doi:10.1038/385329a0.

Cannat, M. (1993), Emplacement of mantle rocks in the seafloor at mid-ocean ridges, *J. Geophys. Res.*, *98*, 4163–4172, doi:10.1029/92JB02221.

Cannat, M., et al. (1995), Thin crust, ultramafic exposures, and rugged faulting patterns at the Mid-Atlantic Ridge (22°–24°N), *Geology*, *23*, 49–52, doi:10.1130/0091-7613(1995)023<0049:TCUEAR>2.3.CO;2.

Cannat, M., Y. Lagabrielle, H. Bougault, J. Casey, N. de Coutures, L. Dmitriev, and Y. Fouquet (1997), Ultramafic and gabbroic exposures of the Mid-Atlantic Ridge: Geological mapping of the 15°N region, *Tectonophysics*, *279*, 193–213.

Cannat, M., J. Cann, and J. Maclennan (2004), Some hard rock constraints on the supply of heat to mid-ocean ridges, in *Mid-Ocean Ridges: Hydrothermal Interactions Between the Lithosphere and Oceans*, *Geophys. Monogr. Ser.*, vol. 148, edited by C. R. German et al., pp. 111–149, AGU, Washington, D. C.

Carbotte, S. M., et al. (2006), Rift topography linked to magmatism at the intermediate spreading Juan de Fuca Ridge, *Geology*, *34*, 209–212, doi:10.1130/G21969.1.

Chadwick, W. W., and R. W. Embley (1998), Graben formation associated with recent dike intrusions and volcanic eruptions on the mid-ocean ridge, *J. Geophys. Res.*, *103*, 9807–9825, doi:10.1029/97JB02485.

Charlou, J. L., J. P. Donval, Y. Fouquet, P. Jean-Baptiste, and N. Holm (2002), Geochemistry of high H2 and CH4 vent fluids issuing from ultramafic rocks at the Rainbow hydrothermal field (36°14′N, MAR), *Chem. Geol.*, *191*, 345–359, doi:10.1016/S0009-2541(02)00134-1.

Chen, Y., and W. J. Morgan (1990), A nonlinear rheology model for mid-ocean ridge axis topography, *J. Geophys. Res.*, *95*, 17,583–17,604, doi:10.1029/JB095iB11p17583.

Cherkashev, G. A., A. M. Ashadze, and A. V. Gebruk (2000), New fields with manifestations of hydrothermal activity in the Logatchev area (14°N, Mid Atlantic Ridge), *InterRidge News*, *9*, 26–27.

Connelly, D. P., C. R. German, M. Asada, K. Okino, A. Egorov, T. Naganuma, N. Pimenov, G. Cherkashev, and K. Tamaki (2007), Hydrothermal activity on the ultra-slow spreading southern Knipovich Ridge, *Geochem. Geophys. Geosyst.*, *8*, Q08013, doi:10.1029/2007GC001652.

Cundall, P. A. (1982), Adaptive density-scaling for time-explicit calculations, in *4th International Conference on Numerical Methods in Geomechanics, Edmonton, Canada*, vol. 1, pp. 23–26, A. A. Balkema, Rotterdam, Netherlands.

Cundall, P. A. (1989), Numerical experiments on localization in frictional materials, *Ing. Arch.*, *59*, 148–159, doi:10.1007/BF00538368.

Curewitz, D., and J. A. Karson (1998), Geological consequences of dike intrusion at mid-ocean ridge spreading centers, in *Faulting and Magmatism at Mid-Ocean Ridges*, *Geophys. Monogr. Ser.*, vol. 106, edited by W. R. Buck et al., pp. 117–136, AGU, Washington, D. C.

deMartin, B. J., R. A. Sohn, J. P. Canales, and S. E. Humphris (2007), Kinematics and geometry of active detachment faulting beneath the Trans-Atlantic Geotraverse (TAG) hydrothermal field on the Mid-Atlantic Ridge, *Geology*, *35*, 711–714, doi:10.1130/G23718A.1.

Detrick, R. S., et al. (1987), Multichannel seismic imaging of the crustal magma chamber along the East Pacific Rise, *Nature*, *326*, 35–41, doi:10.1038/326035a0.

Detrick, R. S., H. D. Needham, and V. Renard (1995), Gravity anomalies and crustal thickness variations along the Mid-Atlantic Ridge between 33°N and 40°N, *J. Geophys. Res.*, *100*, 3767–3787, doi:10.1029/94JB02649.

Detrick, R. S., J. M. Sinton, G. Ito, J. P. Canales, M. Behn, T. Blacic, B. Cushman, J. E. Dixon, D. W. Graham, and J. J. Mahoney (2002), Correlated geophysical, geochemical, and volcanological manifestations of plume-ridge interaction along the Galápagos Spreading Center, *Geochem. Geophys. Geosyst.*, *3*(10), 8501, doi:10.1029/2002GC000350.

Dick, H. J. B., et al. (1991), Tectonic evolution of the Atlantis II Fracture Zone, *Proc. Ocean Drill. Program Sci. Results*, *118*, 359–398.

Dick, H. J. B., et al. (2000), A long in situ section of the lower ocean crust: Results of ODP Leg 176 drilling at the Southwest Indian Ridge, *Earth Planet. Sci. Lett.*, *179*, 31–51, doi:10.1016/S0012-821X(00)00102-3.

Escartín, J., G. Hirth, and B. Evans (1997), Effects of serpentinization on the lithospheric strength and the style of normal faulting at slow-spreading ridges, *Earth Planet. Sci. Lett.*, *151*, 181–189, doi:10.1016/S0012-821X(97)81847-X.

Escartín, J., et al. (1999), Quantifying tectonic strain and magmatic accretion at a slow spreading ridge segment, Mid-Atlantic Ridge, 29°N, *J. Geophys. Res.*, *104*, 10,421–10,437, doi:10.1029/1998JB900097.

Escartín, J., C. Mével, C. J. MacLeod, and A. M. McCaig (2003), Constraints on deformation conditions and the origin of oceanic detachments: The Mid-Atlantic Ridge core complex at 15°45′N, *Geochem. Geophys. Geosyst.*, *4*(8), 1067, doi:10.1029/2002GC000472.

Fialko, Y. A., and A. M. Rubin (1998), Thermodynamics of lateral dike propagation: Implications for crustal accretion at slow spreading mid-ocean ridges, *J. Geophys. Res.*, *103*, 2501–2514, doi:10.1029/97JB03105.

Forsyth, D. W. (1992), Finite extension and low-angle normal faulting, *Geology*, *20*, 27–30, doi:10.1130/0091-7613(1992)020<0027:FEALAN>2.3.CO;2.

German, C. R., and J. Lin (2004), The thermal structure of the oceanic crust, ridge spreading, and hydrothermal circulation: How well do we understand their inter-connections?, in *Mid-Ocean Ridges: Hydrothermal Interactions Between the Lithosphere and Oceans*, *Geophys. Monogr. Ser.*, vol. 148, edited by C. R. German et al., pp. 1–18, AGU, Washington, D. C.

German, C. R., E. T. Baker, C. Mevel, K. Tamaki, and F. S. Team (1998), Hydrothermal activity along the southwest Indian Ridge, *Nature*, *395*, 490–493, doi:10.1038/26730.

Gillis, K. M., G. Thompson, and D. S. Kelley (1993), A view of the lower crustal component of hydrothermal systems at the Mid-Atlantic Ridge, *J. Geophys. Res.*, *98*, 19,597–19,620, doi:10.1029/93JB01717.

Goff, J. A. (1991), A global and regional stochastic analysis of near-ridge abyssal hill morphology, *J. Geophys. Res.*, *96*, 21,713–21,737, doi:10.1029/91JB02275.

Goff, J. A., Y. Ma, A. Shah, J. R. Cochran, and J.-C. Sempéré (1997), Stochastic analysis of seafloor morphology on the flank of the Southeast Indian Ridge: The influence of ridge morphology on the formation of abyssal hills, *J. Geophys. Res.*, *102*, 15,521–15,534, doi:10.1029/97JB00781.

Hassani, R., and J. Chéry (1996), Anelasticity explains topography associated with Basin and Range normal faulting, *Geology*, *24*, 1095–1098, doi:10.1130/0091-7613(1996)024<1095:AETAWB>2.3.CO;2.

Hofton, M. A., and G. Foulger (1996), Postrifting anelastic deformation around the spreading plate boundary, north Iceland 2. Implications of the model derived from the 1987–1992 deformation field, *J. Geophys. Res.*, *101*, 25,423–25,436, doi:10.1029/96JB02465.

Hooft, E. E. E., H. Schouten, and R. S. Detrick (1996), Constraining crustal emplacement processes from the variation of seismic layer 2A thickness at the East Pacific Rise, *Earth Planet. Sci. Lett.*, *142*, 289–310, doi:10.1016/0012-821X(96)00101-X.

Hooft, E. E. E., R. S. Detrick, D. R. Toomey, J. A. Collins, and J. Lin (2000), Crustal thickness and structure along three contrasting spreading segments of the Mid-Atlantic Ridge, 33.5°–35°N, *J. Geophys. Res.*, *105*, 8205–8226, doi:10.1029/1999JB900442.

Hosford, A., J. Lin, and R. S. Detrick (2001), Crustal evolution over the last 2 m.y. at the Mid-Atlantic Ridge OH-1 segment, 35°N, *J. Geophys. Res.*, *106*, 13,269–13,285, doi:10.1029/2001JB000235.

Ildefonse, B., D. K. Blackman, B. E. John, Y. Ohara, D. J. Miller, C. J. MacLeod, and the IODP Expeditions 304/305 Science Party (2007), Oceanic core complexes and crustal accretion at slow-spreading ridges, *Geology*, *35*, 623–626, doi:10.1130/G23531A.1.

Ito, G., and M. D. Behn (2008), Magmatic and tectonic extension at mid-ocean ridges: 2. Origin of axial morphology, *Geochem. Geophys. Geosyst.*, doi:10.1029/2008GC001970, in press.

Jaeger, J. C., and N. G. Cook (1979), *Fundamentals of Rock Mechanics*, 513 pp., Chapman and Hall, London.

Karson, J. A., and H. J. B. Dick (1983), The tectonics of ridge-transform intersections at the Kane fracture zone, *Mar. Geophys. Res.*, *6*, 51–98, doi:10.1007/BF00300398.

Kirby, S. H. (1983), Rheology of the Lithosphere, *Rev. Geophys.*, *21*, 1458–1487, doi:10.1029/RG021i006p01458.

Kohlstedt, D. L., B. Evans, and S. J. Mackwell (1995), Strength of the lithosphere: Constraints imposed by laboratory experiments, *J. Geophys. Res.*, *100*, 17,587–17,602, doi:10.1029/95JB01460.

Kong, L. S. L., S. C. Solomon, and G. M. Purdy (1992), Microearthquake characteristics of a Mid-Ocean Ridge along-axis high, *J. Geophys. Res.*, *97*, 1659–1685, doi:10.1029/91JB02566.

Kuo, B., and D. W. Forsyth (1988), Gravity anomalies of the ridge-transform system in the South Atlantic between 31° and 34.5°S: Upwelling centers and variations in crustal thickness, *Mar. Geophys. Res.*, *10*, 205–232, doi:10.1007/BF00310065.

Lavier, L. L., and W. R. Buck (2002), Half graben versus large-offset low-angle normal fault: Importance of keeping cool during normal faulting, *J. Geophys. Res.*, *107*(B6), 2122, doi:10.1029/2001JB000513.

Lavier, L. L., W. R. Buck, and A. N. B. Poliakov (2000), Factors controlling normal fault offset in an ideal brittle layer, *J. Geophys. Res.*, *105*, 23,431–23,442, doi:10.1029/2000JB900108.

Lin, J., G. M. Purdy, H. Schouten, J.-C. Sempéré, and C. Zervas (1990), Evidence from gravity data for focused magmatic accretion along the Mid-Atlantic ridge, *Nature*, *344*, 627–632, doi:10.1038/344627a0.

Lister, C. R. B. (1974), On the penetration of water into hot rock, *Geophys. J. R. Astron. Soc.*, *39*, 465–509.

Macdonald, K. C. (1982), Mid-ocean ridges: Fine scale tectonic, volcanic and hydrothermal processes within the plate boundary zone, *Annu. Rev. Earth Planet. Sci.*, *10*, 155–190, doi:10.1146/annurev.ea.10.050182.001103.

Macdonald, K. C. (1986), The crest of the Mid-Atlantic Ridge: Models for crustal generation processes and tectonics, in *The Geology of North America,* vol. M, *The Western North Atlantic Region*, edited by P. R. Vogt and B. E. Tucholke, pp. 51–68, Geol. Soc. of Am., Boulder, Colo.

Macdonald, K. C., and P. J. Fox (1988), The axial summit graben and cross-sectional shape of the East Pacific Rise as indicators of axial magma chambers and recent volcanic eruptions, *Earth Planet. Sci. Lett.*, *88*, 119–131, doi:10.1016/0012-821X(88)90051-9.

Mackwell, S. J., M. E. Zimmerman, and D. L. Kohlstedt (1998), High-temperature deformation of dry diabase with application to tectonics on Venus, *J. Geophys. Res.*, *103*, 975–984, doi:10.1029/97JB02671.

Malinverno, A., and P. A. Cowie (1993), Normal faulting and the topographic roughness of mid-ocean ridge flanks, *J. Geophys. Res.*, *98*, 17,921–17,939, doi:10.1029/93JB01571.

Martinez, F., B. Taylor, E. T. Baker, J. A. Resing, and S. L. Walker (2006), Opposing trends in crustal thickness and spreading rate along the back-arc Eastern Lau Spreading Center: Implications for controls on ridge morphology, faulting, and hydrothermal activity, *Earth Planet. Sci. Lett.*, *245*, 655–672, doi:10.1016/j.epsl.2006.03.049.

Mastin, L. G., and D. D. Pollard (1988), Surface deformation and shallow dike intrusion processes at Inyo Craters, Long Valley, California, *J. Geophys. Res.*, *93*, 13,221–13,235, doi:10.1029/JB093iB11p13221.

Melosh, H. J., and C. A. Williams Jr. (1989), Mechanics of graben formation in crustal rocks: A finite element analysis, *J. Geophys. Res.*, *94*, 13,961–13,973, doi:10.1029/JB094iB10p13961.

Natland, J. H., and H. J. B. Dick (2001), Formation of the lower ocean crust and the crystallization of gabbroic cumulates at a very slowly spreading ridge, *J. Volcanol. Geotherm. Res.*, *110*, 191–233, doi:10.1016/S0377-0273(01)00211-6.

Neumann, G. A., and D. W. Forsyth (1993), The paradox of the axial profile: Isostatic compensation along the axis of the mid-Atlantic ridge?, *J. Geophys. Res.*, *98*, 17,891–17,910, doi:10.1029/93JB01550.

Phipps Morgan, J., and Y. J. Chen (1993), The genesis of oceanic crust: Magma injection, hydrothermal circulation, and crustal flow, *J. Geophys. Res.*, *98*, 6283–6297, doi:10.1029/92JB02650.

Phipps Morgan, J., and D. W. Forsyth (1988), Three-dimensional flow and temperature perturbations due to a transform offset: Effects on oceanic crust and upper mantle structure, *J. Geophys. Res.*, *93*, 2955–2966, doi:10.1029/JB093iB04p02955.

Phipps Morgan, J., E. M. Parmentier, and J. Lin (1987), Mechanisms for the origin of mid-ocean ridge axial topography: Implications for the thermal and mechanical structure of accreting plate boundaries, *J. Geophys. Res.*, *92*, 12,823–12,836, doi:10.1029/JB092iB12p12823.

Poliakov, A. N. B., and W. R. Buck (1998), Mechanics of stretching elastic-plastic-viscous layers: Applications to slow-spreading mid-ocean ridges, in *Faulting and Magmatism at Mid-Ocean Ridges*, *Geophys. Monogr. Ser.*, vol. 106, edited by W. R. Buck et al., pp. 305–323, AGU, Washington, D. C.

Poliakov, A. N. B., P. A. Cundall, Y. Y. Podladchikov, and V. A. Lyakhovsky (1993), An explicit inertial method for the simulation of viscoelastic flow: An evaluation of elastic effects on diapiric flow in two- and three-layer models, in *Flow and Creep in the Solar System: Observations, Modeling and Theory*, edited by D. B. Stone and S. K. Runcorn, pp. 175–195, Kluwer Acad., Dordrecht, Netherlands.

Pollard, D. D., P. T. Delaney, W. A. Duffield, E. T. Endo, and A. T. Okamura (1983), Surface deformation in volcanic rift zones, *Tectonophysics*, *94*, 541–584, doi:10.1016/0040-1951(83)90034-3.

Rubin, A. M. (1992), Dike-induced faulting and graben subsidence in volcanic rift zones, *J. Geophys. Res.*, *97*, 1839–1858, doi:10.1029/91JB02170.

Rubin, A. M., and D. D. Pollard (1988), Dike-induced faulting in rift zones of Iceland and Afar, *Geology*, *16*, 413–417, doi:10.1130/0091-7613(1988)016<0413:DIFIRZ>2.3.CO;2.

Searle, R. C., and A. S. Laughton (1981), Fine-scale sonar study of tectonics and volcanism on the Reykjanes Ridge, *Oceanol. Acta*, *4*, suppl., 5–13.

Shaw, P. R. (1992), Ridge segmentation, faulting and crustal thickness in the Atlantic Ocean, *Nature*, *358*, 490–493, doi:10.1038/358490a0.

Shaw, P. R., and J. Lin (1993), Causes and consequences of variations in faulting style at the Mid-Atlantic Ridge, *J. Geophys. Res.*, *98*, 21,839–21,851, doi:10.1029/93JB01565.

Shaw, W. J., and J. Lin (1996), Models of ocean ridge lithospheric deformation: Dependence on crustal thickness, spreading rate, and segmentation, *J. Geophys. Res.*, *101*, 17,977–17,993, doi:10.1029/96JB00949.

Shen, Y., and D. W. Forsyth (1992), The effects of temperature- and pressure-dependent viscosity on three-dimensional passive flow of the mantle beneath a ridge-transform system, *J. Geophys. Res.*, *97*, 19,717–19,728, doi:10.1029/92JB01467.

Sigurdsson, O. (1980), Surface deformation of the Krafla fissure swarm in two rifting events, *J. Geophys.*, *47*, 154–159.

Singh, S. C., G. M. Kent, J. S. Collier, A. J. Harding, and J. A. Orcutt (1998), Melt to mush variations in crustal magma properties along the ridge crest at the southern East Pacific Rise, *Nature*, *394*, 874–878, doi:10.1038/29740.

Singh, S. C., et al. (2006), Discovery of a magma chamber and faults beneath a Mid-Atlantic Ridge hydrothermal field, *Nature*, *442*, 1029–1032, doi:10.1038/nature05105.

Sinton, J., R. Detrick, J. P. Canales, G. Ito, and M. Behn (2003), Morphology and segmentation of the western Galápagos Spreading Center, 90.5°–98°W: Plume-ridge interaction at an intermediate spreading ridge, *Geochem. Geophys. Geosyst.*, *4*(12), 8515, doi:10.1029/2003GC000609.

Sleep, N. H. (1975), Formation of oceanic crust: Some thermal constraints, *J. Geophys. Res.*, *80*, 4037–4042, doi:10.1029/JB080i029p04037.

Small, C. (1998), Global systematics of mid-ocean ridge morphology, in *Faulting and Magmatism at Mid-Ocean Ridges*, *Geophys. Monogr. Ser.*, vol. 106, edited by W. R. Buck et al., pp. 1–25, AGU, Washington, D. C.

Smith, D. K., and J. R. Cann (1993), Building the crust at the Mid-Atlantic Ridge, *Nature*, *365*, 707–715, doi:10.1038/365707a0.

Smith, D. K., J. Escartin, M. Cannat, M. Tolstoy, C. G. Fox, D. R. Bohnenstiehl, and S. Bazin (2003), Spatial and temporal distribution of seismicity along the northern Mid-Atlantic Ridge (15°–35°N), *J. Geophys. Res.*, *108*(B3), 2167, doi:10.1029/2002JB001964.

Solomon, S. C., P. Y. Huang, and L. Meinke (1988), The seismic moment budget of slowly spreading ridges, *Nature*, *334*, 58–60, doi:10.1038/334058a0.

Tolstoy, M., A. J. Harding, and J. A. Orcutt (1993), Crustal thickness on the Mid-Atlantic Ridge: Bull's-eye gravity anomalies and focused accretion, *Science*, *262*, 726–729, doi:10.1126/science.262.5134.726.

Toomey, D. R., S. C. Solomon, and G. M. Purdy (1988), Microearthquakes beneath median valley of Mid-Atlantic Ridge near 23°N: Tomography and tectonics, *J. Geophys. Res.*, *93*, 9093–9112, doi:10.1029/JB093iB08p09093.

Tucholke, B. E., and J. Lin (1994), A geological model for the structure of ridge segments in slow spreading ocean crust, *J. Geophys. Res.*, *99*, 11,937–11,958, doi:10.1029/94JB00338.

Tucholke, B. E., et al. (1997), Segmentation and crustal structure of the western Mid-Atlantic Ridge flank, 25°25′–27°10′N and 0–29 m.y, *J. Geophys. Res.*, *102*, 10,203–10,223, doi:10.1029/96JB03896.

Tucholke, B. E., J. Lin, and M. C. Kleinrock (1998), Megamullions and mullion structure defining oceanic metamorphic core complexes on the mid-Atlantic ridge, *J. Geophys. Res.*, *103*, 9857–9866, doi:10.1029/98JB00167.

Tucholke, B. E., K. Fujioka, T. Ishihara, G. Hirth, and M. Kinoshita (2001), Submersible study of an oceanic megamullion in the central North Atlantic, *J. Geophys. Res.*, *106*, 16,145–16,161, doi:10.1029/2001JB000373.

Tucholke, B. E., M. D. Behn, W. R. Buck, and J. Lin (2008), Role of melt supply in oceanic detachment faulting and formation of megamullions, *Geology*, *36*, 455–458, doi:10.1130/G24639A.1.

Van Ark, E. M., R. S. Detrick, J. P. Canales, S. M. Carbotte, A. J. Harding, G. M. Kent, M. R. Nedimovic, W. S. D. Wilcock, J. B. Diebold, and J. M. Babcock (2007), Seismic structure of the Endeavour Segment, Juan de Fuca Ridge: Correlations with seismicity and hydrothermal activity, *J. Geophys. Res.*, *112*, B02401, doi:10.1029/2005JB004210.

Wessel, P., and W. H. F. Smith (1995), New version of the generic mapping tools released, *Eos Trans. AGU*, *76*(33), 329.

Wilcock, W. S. D., and J. R. Delaney (1996), Mid-ocean ridge sulfide deposits: Evidence for heat extraction from magma chambers or cracking fronts, *Earth Planet. Sci. Lett.*, *145*, 49–64, doi:10.1016/S0012-821X(96)00195-1.

Wolfe, C. J., G. M. Purdy, D. R. Toomey, and S. C. Solomon (1995), Microearthquake characteristics and crustal velocity structure at 29°N on the Mid-Atlantic Ridge: The architecture of a slow spreading segment, *J. Geophys. Res.*, *100*, 24,449–24,472, doi:10.1029/95JB02399.

Wright, T. L., et al. (2006), Magma-maintained rift segmentation at continental rupture in the 2005 Afar dyking episode, *Nature*, *442*, 291–294, doi:10.1038/nature04978.